Published in final edited form as:
Curr Biol. 2021 March 22; 31(6): 1141–1153.e7. doi:10.1016/j.cub.2020.12.006.

Actin at stereocilia tips is regulated by mechanotransduction and ADF/cofilin

Jamis McGrath[1], **Chun-Yu Tung**[1], **Xiayi Liao**[1], **Inna A Belyantseva**[2], **Pallabi Roy**[1], **Oisorjo Chakraborty**[1], **Jinan Li**[5], **Nicolas F Berbari**[1], **Christian Faaborg-Anderson**[2], **Melanie Barzik**[3],

[*]Correspondence: bperrin@iupui.edu.

AUTHOR CONTRIBUTIONS
Conceptualization: JM and BJP
Methodology: JM, NFB, and BJP
Investigation: JM, CT, XL, IB, PR, CO, CFA, MB, JEB, LB, and BJP
Resources: JL, BZ, LB, and TBF
Writing: JM, IB, JEB, TBF, and BJP
Funding acquisition: TBF and BJP

DECLARATION OF INTERESTS:
The authors have no conflicts of interest to declare.

Sample sizes
Figure 1C: We used 19 cells from 3 C57BL/6 mice at P3-P4 for FRAP analysis.
Figure 2C-D: Two or more images were taken of the sensory epithelium in both cochlea of at least 3 mice per timepoint.
Figure 2F-G: For IHCs: row 1, n = 36 cells; row 2, n = 36 cells; row 3, n = 35 cells. For OHCs: row 1, n = 42 cells; row 2, n = 41 cells; row 3, n = 40 cells. We used 2 P6 $Adf^{-/+}$ $Cfl1^{fl/+}$ control mice to measure rhodamine-actin incorporation.
Figure 3C: For both rows, 61 and 58 cells were quantified in $Tmie^{+/-}$ controls and $Tmie^{-/-}$ mutants, respectively.
Figure 3F-G: Explants were generated from 6 littermate C57BL/6 mice, and half were used for either rhodamine-actin or EPS8 labeling. The two experiments were performed simultaneously to eliminate differences caused by age or treatment time. (Panel F) Ratios of available barbed ends were determined from 25 and 22 IHCs from control and tubocurarine treated explants. (Panel G) Ratios of EPS8 labeling were determined from 25 and 31 IHCs from control and tubocurarine treated explants.
Figure 5D: For both rows, 42 and 44 cells were quantified in $Eps8^{+/-}$ (controls) and $Eps8^{-/-}$ (mutants), respectively. Three mice from each condition, controls and mutants, were used.
Figure 6D: For both rows, 42 and 44 cells were quantified in $Adf^{+/-}$ $Cfl1^{fl/+}$ (controls) and $Adf^{-/-}$ $Cfl1^{fl/+}$ *Atoh1-cre* (mutants), respectively. Four controls and five mutants were used for quantification.
Figure 7C: Length measurements were performed on IHCs of $Adf^{+/-}$ $Cfl1^{fl/fl}$ (controls) and $Adf^{-/-}$ $Cfl1^{fl/fl}$ *Cagg-creER* (iDKO) For controls: row 1, n = 36 cells; row 2, n = 36 cells; row 3, n = 35 cells. For iDKO: row 1, n = 42 cells; row 2, n = 41 cells; row 3, n = 40 cells. Four mice from each condition, controls and mutants, were used for quantification at P5, three days after tamoxifen dose.
Figure 7D: In order to show comparable distributions and means for $Adf^{+/-}$ $Cfl1^{fl/fl}$ (controls) and $Adf^{-/-}$ $Cfl1^{fl/fl}$ *Cagg-creER* (iDKOs), values were displayed for each stereocilia. For controls: row 1, n = 503 stereocilia; row 2, n = 436 stereocilia; from 38 cells, averaging 9.5 cells per mouse. For iDKOs: row 1, n = 418 stereocilia; row 2, n = 361 stereocilia; from 31 cells, averaging 7.75 cells per mouse. Four mice from each condition, controls and mutants, were used for quantification at P5, three days after tamoxifen dose.
Figure 7E: For $Adf^{+/-}$ $Cfl1^{fl/fl}$ (controls) IHCs: row 1, n = 21 cells; row 2, n = 15 cells; row 3, n = 21 cells. For $Adf^{-/-}$ $Cfl1^{fl/fl}$ *Cagg-creER* (iDKO) IHCs: row 1, n = 15 cells; row 2, n = 21 cells; row 3, n = 15 cells. For controls OHCs: row 1, n = 27 cells; row 2, n = 16 cells; row 3, n = 27 cells. For iDKO OHCs: row 1, n = 16 cells; row 2, n = 27 cells; row 3, n = 16 cells. Two mice from each condition, controls and iDKOs, were used for quantification at P5, three days after tamoxifen dose.
Figure S1C: Ratio of rhodamine-actin fluorescence intensities from 11 and 22 cells of control and tubocurarine treated explants. Three mice were used for each condition, controls and treated.
Figure S1D: Ratio of EPS8 fluorescence intensities from 24 and 26 cells of control and tubocurarine treated explants. Three mice were used for each condition, controls and treated.
Figure S1G: Ratio of EPS8 fluorescence intensities from 19 and 11 cells of control and tubocurarine treated explants. Three mice were used for each condition, controls and treated.
Figure S4C: For $Adf^{+/-}$ $Cfl1^{fl/+}$ (control) IHCs: row 1, n = 14 cells; row 2, n = 13 cells; row 3, n = 14 cells; row 4, n = 14 cells. For $Adf^{-/-}$ $Cfl1^{fl/+}$ *Atoh1-cre* (mutant) IHCs: row 1, n = 20 cells; row 2, n = 19 cells; row 3, n = 20 cells; row 4, n = 20 cells. Three mice were used for each condition, controls and mutants.
Figure S5B: Ratio of rhodamine-actin fluorescence intensities from $Adf^{+/-}$ $Cfl1^{fl/fl}$ (control) and $Adf^{-/-}$ $Cfl1^{fl/fl}$ *Cagg-creER* (iDKO) IHCs. For controls and mutants: n = 21 cells from one mouse for each condition.

Jonathan E Bird[4], **Bo Zhao**[5], **Lata Balakrishnan**[1], **Thomas B Friedman**[2], **Benjamin J Perrin**[1,6,*]

[1]Department of Biology, Indiana University-Purdue University 723 W. Michigan St., Indianapolis, Indianapolis, IN 46202, USA

[2]Laboratory of Molecular Genetics, National Institute of Deafness and Other Communication Disorders, NIH, 35 Convent Dr., Bethesda, MD 20892, USA

[3]Section on Sensory Cell Biology, National Institute of Deafness and Other Communication Disorders, NIH, 35 Convent Dr., Bethesda, MD 20892, USA

[4]Department of Pharmacology and Therapeutics, University of Florida, 1200 Newell Dr., Gainesville, FL 32610, USA

[5]Department of Otolaryngology-Head and Neck Surgery, Indiana University School of Medicine, 1160 W. Michigan St., Indianapolis, IN 46202, USA

[6]Lead Contact

SUMMARY:

Stereocilia on auditory sensory cells are actin-based protrusions that mechanotransduce sound into an electrical signal. These stereocilia are arranged into a bundle with three rows of increasing length to form a staircase-like morphology that is required for hearing. Stereocilia in the shorter rows, but not the tallest row, are mechanotransducing because they have force sensitive channels localized at their tips. The onset of mechanotransduction during mouse postnatal development refines stereocilia length and width. However, it is unclear how actin is differentially regulated between stereocilia in the tallest row of the bundle and the shorter, mechanotransducing rows. Here we show actin turnover is increased at the tips of mechanotransducing stereocilia during bundle maturation. Correspondingly, from birth to postnatal day 6, these stereocilia had increasing amounts of available actin barbed ends, where monomers can be added or lost readily, as compared to the non-mechanotransducing stereocilia in the tallest row. The increase in available barbed ends depended on both mechanotransduction and MYO15 or EPS8, which are required for the normal specification and elongation of the tallest row of stereocilia. We also found that loss of the F-actin severing proteins ADF and cofilin-1 decreased barbed end availability at stereocilia tips. These proteins enriched at mechanotransducing stereocilia tips and their localization was perturbed by the loss of mechanotransduction, MYO15, or EPS8. Finally, stereocilia lengths and widths were dysregulated in *Adf* and *Cfl1* mutants. Together, these data show that actin is remodeled, likely by a severing mechanism, in response to mechanotransduction.

Keywords

Stereocilia; mechanotransduction; actin; cofilin; ADF; development; morphogenesis; protrusion; morphology

INTRODUCTION:

Sensory hair cells of the inner ear have mechanosensory protrusions on their apical surface called stereocilia, which convert force from sound or acceleration into electrical signals that are subsequently processed by the central nervous system. In auditory hair cells, three rows of stereocilia, each of ascending height, with row 1 being the tallest, are arranged to produce a bundle with a precise staircase-like morphology [1]. The shape of the bundle is intrinsically linked with its function. Mechanotransduction channels, located near the tips of stereocilia in the shorter two rows, are gated by tip links that connect to stereocilia in the adjacent, taller row [2–4]. When the stereocilia bundle is deflected by sound towards the tallest row, force is transmitted through the tip links to mechanotransducing stereocilia in the shorter row, which have force sensitive ion channels that open, resulting in an influx of K^+ and Ca^{2+}. Since stereocilia are required to sense sound, defects in their development and maintenance cause hearing loss.

The dimensions of stereocilia are determined by their actin cores, which consists of a bundle of highly crosslinked, parallel actin filaments (F-actin) oriented with their barbed ends towards stereocilia tips [5]. The barbed end of an actin filament is the fast-growing end since actin monomers have a higher affinity for this rapidly polymerizing end compared with the slower-growing pointed end [6–9]. While many actin networks, such as those that form protrusive structures like lamellipodia and microvilli, are characterized by high F-actin turnover featuring a so-called actin “treadmill” [10–13], the F-actin in stereocilia is exceptionally stable. As stereocilia elongate during development, actin stably incorporates into the growing actin core at stereocilia tips. In mature stereocilia, actin turnover is largely restricted to their tips, where the barbed ends of filament reside, with limited incorporation along the stereocilia length [14–16].

Several factors are known to control normal actin assembly in developing stereocilia. The myosin-15 (MYO15) complex, which includes the actin binding protein epidermal growth factor receptor substrate 8 (EPS8), whirlin (WHRN), G-protein signaling modulator (GPSM2), and guanine nucleotide binding protein G(i) subunit alpha-1 (GNAI), becomes enriched at the tips of stereocilia in the tallest row and is essential for their elongation [17–22]. Other proteins, including EPS8-like 2 (EPS8L2) and the long splice isoform of MYO15, are conversely enriched at the tips of shorter row stereocilia [23]. Thus, stereocilia in row 1, the tallest row, and those in the shorter, mechanotransducing rows (rows 2 and 3) have distinct protein complexes at their tips that likely control actin dynamics during development to set their lengths and widths [24, 25]. The maintenance of row specific signaling networks initially depends on mechanotransduction [24], which begins around P0 in the base and P2 in the apex in mice and rats [26, 27]. When mechanotransduction is blocked, the proteins that are normally enriched in taller or shorter rows are more evenly distributed, and stereocilia lengths and widths are correspondingly dysregulated [24, 28]. Later in development, loss of tip links or mechanotransduction results in shortening and eventual loss of mechanotransducing stereocilia [29–31]. Thus, initial sorting of row specific proteins, reinforced by mechanotransduction activity, is required to produce and maintain a normal stereocilia bundle.

We hypothesize that row-specific proteins localized at stereocilia tips respond to mechanotransduction to regulate the availability of F-actin barbed ends, the filament end that most readily polymerizes new monomers. Barbed end availability is determined by the combined actions of actin nucleators that initiate actin polymerization, capping proteins that bind and obscure filament barbed ends, and actin severing proteins, which generate a new barbed end at each filament break point. Twinfilin-2 (TWF2), CAPZ, and EPS8 have barbed end capping activity [32–34], localize to stereocilia tips and regulate stereocilia morphology [20, 35–37]. The severing protein actin depolymerizing factor (ADF, or DSTN) and actin interacting protein 1 (AIP1, or WDR1), which potentiates actin severing, are required to maintain the lengths of mechanotransducing stereocilia [15]. However, the effects of severing remain unclear because the paralogous protein cofilin-1 (CFL1), which shares 70% sequence identity with ADF, is ubiquitously expressed and likely compensates for the loss of ADF [38].

Our data show that stereocilia in the shorter rows of the bundle had more actin turnover at their tips than those in the tallest row, which corresponded with higher levels of available F-actin barbed ends. This population of available barbed ends was progressively enriched at the tips of the shorter stereocilia during postnatal development and depended on ADF and CFL1, the levels of which also increased at mechanotransducing stereocilia tips during the same period of development. The enrichment of free F-actin barbed ends, ADF, and CFL1 required both mechanotransduction and the normal, MYO15-dependent distribution of row-specific stereocilia proteins. Finally, the loss of both ADF and CFL1 had complex effects on stereocilia shape, leading to shorter row 1 stereocilia, generally wider stereocilia, and more tapered mechanotransducing stereocilia in row 3 of the bundle. Together, we found that ADF and CFL1 regulate actin in stereocilia, especially at the tips of stereocilia where they increase the availability of filament barbed ends in response to mechanotransduction.

RESULTS:

During postnatal development in mouse, the regulation of actin dynamics in hair cell stereocilia is not well understood. We first assessed actin incorporation by using a cre-inducible transgene to start actin-EGFP expression following tamoxifen injection on postnatal day 6 (P6). At P28, the actin-EGFP that had incorporated into the stereocilia actin core was visualized by confocal microscopy. This transgene is expressed at different levels between cells, explaining the variable extent of incorporation (Figure 1A) [15]. In inner hair cells (IHCs), actin-EGFP was detected in row 1 stereocilia (the tallest row) along a segment extending down from the tip suggesting that actin-EGFP was stably incorporated into the elongating core (Figure 1A, arrows), a similar pattern to that previously observed in vestibular hair cell stereocilia [16]. In contrast, in row 2 stereocilia actin-EGFP incorporation was predominantly limited to their tips (Figure 1A, arrowheads), which are shorter and were done elongating before actin-EGFP expression started [24]. Together, these data show that actin regulation differs between stereocilia in the tallest row and those in the shorter, mechanotransducing rows.

Following induction, actin-EGFP incorporation into stereocilia is not evident for several hours so more rapid changes in actin dynamics cannot be observed. To assess the actin

dynamics of row 1 and row 2 stereocilia tips with better time resolution, we measured fluorescence recovery after photobleaching (FRAP) of EGFP-actin, which was constitutively expressed in IHCs from a *Myo7a*-promoter regulated transgene, in cultured explants from P3-P4 mice (Figure 1B). This is a different transgenic mouse line than use for Figure 1A, and the EGFP is on the N-terminus of β-actin rather than the C-terminus. Since EGFP-actin was expressed from an early developmental stage, it incorporated along the length of IHC stereocilia as they developed [14, 16]. Following photobleaching of IHC stereocilia, EGFP-actin recovered at the tips of both row 1 and row 2 stereocilia but not along the shafts, showing that actin is incorporated at the tips but is comparatively stable in IHC stereocilia shafts during early postnatal development. We also observed that actin behaves differently at the tips of row 1 and row 2 stereocilia. After photobleaching, EGFP-actin fluorescence recovered to higher levels at row 2 tips than at row 1 tips, suggesting that this population has a greater mobile fraction of actin (Figure 1B, C). This difference in fluorescence recovery may depend in part on how fast actin monomers reach the tips of long or shorter stereocilia as well as reflect differences in the dynamic behavior of actin networks at stereocilia tips.

We next sought to characterize potential differences in the actin network at stereocilia tips by assessing the availability of F-actin barbed ends. A snapshot of barbed end availability has been measured in other cellular systems by adding labeled, monomeric actin (G-actin) to cells permeabilized with the detergent saponin [39]. The labeled actin adds to the free, unoccupied barbed ends of existing filaments but not to barbed ends blocked by capping proteins. We first tested this methodology by determining whether exogenous proteins could gain access to the stereocilia core following permeabilization of unfixed, freshly dissected inner ear tissue with 0.05% saponin. Purified Flag-tagged fascin-1 (FSCN1) localized along the entire length of stereocilia in permeabilized inner hair cells of P5 organ of Corti (Figure 2A, B), showing that the structure was accessible to exogenous proteins, and that the endogenous localization pattern of fascin proteins and their ability to exchange within the stereocilia core was preserved in this system [40, 41].

Next, we assessed the availability of F-actin ends between P0 and P6 by incubating saponin permeabilized cochlear tissue in an actin polymerization buffer containing purified, rhodamine-labeled G-actin. Next, samples were fixed and stained with phalloidin to label endogenous F-actin in the stereocilia core. At P0, rhodamine-actin was faintly detected at IHC stereocilia tips with no clear difference in incorporation between rows of stereocilia (Figure 2C). In contrast, at P1, P2, and P6, after the reported onset of mechanotransduction [26], rhodamine-actin was progressively enriched at the tips of stereocilia in the second row as compared to those in the tallest row. By P6, fluorescence intensity of labeled actin at row 2 IHC stereocilia tips was approximately 3-fold higher than at row 1 tips (Figure 2C, F). In P6 outer hair cells (OHCs), labeling was also notably enriched in row 2 stereocilia as compared to either rows 1 or 3 (Figure 2D). In addition, purified His-tagged heterodimeric CAPZα1/β capping protein (CAPZ), which selectively binds to filament barbed ends with high-affinity, also labeled row 2 IHC stereocilia tips more intensely than in row 1 (row 2:row 1 = 2.7), confirming that free barbed ends are more available at mechanotransducing stereocilia tips (Figure 2E). The fluorescence intensity of rhodamine-actin at the tips of stereocilia in rows 1, 2, and 3 from P6 samples was measured and normalized to the average intensity at IHC row 2 tips from the same image (Figure 2F). In both IHCs and OHCs,

row 2 stereocilia had the most rhodamine-actin incorporation in the bundle. The widths of stereocilia in each row vary, so we further normalized rhodamine-actin levels to the cross-sectional area from each row, which was calculated from width measurements taken from scanning electron micrographs of IHC and OHC stereocilia from P5 mice (Figure 2G). Following normalization, the difference in labeling intensities between stereocilia in row 2 and row 3 is reduced, but still significant, even though both rows mechanotransduce [3] (Figure 2G). Though stereocilia in rows 2 and 3 differ, both rows have markedly higher levels of available actin barbed ends than stereocilia in row 1, which lack the mechanotransduction apparatus.

Since barbed end availability was higher at the tips of mechanotransducing stereocilia, we next asked whether mechanotransduction is important for their enrichment. To test this idea, we assessed rhodamine-actin incorporation in stereocilia of rows 1 and 2 in saponin-permeabilized organ of Corti from *Tmie* (Transmembrane inner ear) null mice, which lack detectable mechanotransduction currents [42]. In $Tmie^{-/-}$ hair cells at P6, rhodamine-actin incorporation was markedly reduced in row 2 stereocilia tips and also increased in row 1 stereocilia tips, equalizing levels between the rows (Figure 3A–C). Thus, mechanotransduction and/or channel components are required for increasing the relative availability of free barbed ends in row 2 stereocilia tips.

We next blocked mechanotransduction channels with tubocurarine [24, 31] in explants cultured from P4 C57Bl/6 mice to determine if ion influx is required to generate available actin ends. After 18 hours of treatment, the relative enrichment of rhodamine-actin labeling at row 2 stereocilia tips was nearly abolished such that row 1 and row 2 had equal levels (Figure 3D–F). As revealed by immunostaining, a small fraction of the row 1 complex component EPS8 concurrently distributed to row 2 stereocilia tips (Figure 3G). This shift was statistically significant, though the magnitude of the change in EPS8 localization was much less than that of the shift of free barbed ends away from row 2. The difference in magnitude suggests that barbed end levels change in response to the loss of mechanotransduction and not a more general loss of stereocilia row identity throughout the bundle. No effect on barbed end availability was seen after 6 hours of tubocurarine treatment, suggesting the mechanism connecting mechanotransduction to actin regulation is slow and perhaps indirect (Figure S1A–C).

Regarding the mechanism controlling barbed end availability, we next considered a potential role for the ubiquitously expressed F-actin severing proteins ADF and CFL1. Severing is a possible mechanism because it directly produces new barbed and pointed ends at each break point. In addition, ADF binding along filaments inhibits barbed end capping protein from binding [43]. To determine if ADF/CFL1 co-localized with available F-actin barbed ends at stereocilia tips, we labeled the organ of Corti with an antibody that detects both ADF and CFL1 simultaneously at developmental ages ranging from P0 to P6. Corresponding to the pattern of available barbed ends, ADF/CFL1 were diffusely localized throughout the stereocilia bundle at P0 but became progressively enriched at the tips of IHC row 2 stereocilia from P1 to P6 (Figure 4A). The antibody signal intensity varied between individual tips and could sometimes be seen as two or three distinct puncta (Figure 4B). ADF/CFL1 were also detected in OHC bundles where their localization was also most

evident in row 2 (Figure 4C). In addition, ADF/CFL1 were not enriched in row 2 stereocilia from *Tmie*$^{-/-}$ mice and instead localized as smaller puncta evenly distributed at the tips of stereocilia in all the shorter rows and, to a lesser extent, in row 1 (Figure 4D). Thus, the level of ADF/CFL1 staining correlates with the availability of F-actin barbed ends in both wild type and mutant hair cells. Finally, ADF/CFL1 also localize to the tips of mechanotransducing stereocilia in mature (P26) IHC and OHC bundles (Figure 4E), suggesting these proteins are important for mechanotransduction-dependent actin regulation throughout the life of the cell.

To further understand ADF/CFL1 activity, we assessed their localization and free barbed end production in *Myo15* and *Eps8* mutants. MYO15 and EPS8, along with WHRN, GPSM2, and GNAI, localize predominately to row 1 tips, together forming a tip complex that is required to elongate stereocilia, produce the normal stair-step morphology, and establish the different widths in each row of the bundle [20–22, 25, 37, 44, 45]. We found that ADF/CFL1 were more evenly distributed at the tips of stereocilia in all rows of auditory bundles in the *Myo15*^{sh2} (shaker-2) mutant (Figure 5A), which has a mutation disabling the motor domain common to all isoforms. ADF/CFL1 were similarly mislocalized in auditory stereocilia when *Eps8* was mutated by a 2 or 7 base pair deletion induced by CRISPR/Cas9 (Figure 5B, Figure S2). Rhodamine-actin incorporation in saponin-permeabilized tissue from *Eps8*$^{-/-}$ mice was quantified in IHC stereocilia, demonstrating a reduction at row 2 stereocilia tips and concurrent increase at row 1 tips (40% and 135%, respectively, Figure 5C, D). Changes in ADF/CFL1 localization and barbed end enrichment in *Eps8*$^{-/-}$ row 2 stereocilia resembles that seen in *Tmie*$^{-/-}$ hair cell bundles, where EPS8 is localized to the tips of all rows [24] (Figure 4D, 5C). TMIE, MYO15, and EPS8 are all required to establish the unique molecular identity of mechanotransducing and non-transducing stereocilia, which is therefore likely required for normal ADF/CFL1 localization and activity. After patterning is established, ADF/CFL1, along with other proteins that localize to the tips of row 2/3 stereocilia, are positioned to regulate actin in response to mechanotransduction.

To determine if ADF/CFL1 are required to produce free F-actin barbed ends at stereocilia tips, we next measured rhodamine-actin labeling intensity in stereocilia from *Adf/Cfl1* knockout mutant mice. Mice with a deletion of *Adf* or *Cfl1* had only mild phenotypes related to stereocilia morphology, presumably due to functional compensation between the proteins. We generated hair cells lacking both proteins by using *Atoh1-cre*, which initiates cre expression in IHCs and OHCs between E14 and P4 [46, 47], to delete *Cfl1* in a whole-body *Adf*$^{-/-}$ knockout mouse. These *Adf*$^{-/-}$ *Cfl1*$^{fl/fl}$ *Atoh1-cre* hair cells had severely dysmorphic bundles that were unsuitable for analysis (Figure S3). Therefore, we measured free actin barbed ends in hair cells from *Adf*$^{-/-}$ mice lacking one allele of *Cfl1*. Compared to bundles from control *Adf*$^{-/+}$ *Cfl1*$^{fl/+}$ hair cells, row 2 IHC stereocilia in hair cells from *Adf*$^{-/-}$ *Cfl1*$^{fl/+}$ *Atoh1-cre* mice had 58% less rhodamine-actin incorporation as well as a slight reduction at row 1 tips (Figure 6A–D). A similar pattern was also observed in OHC stereocilia (Figure 6A, B). Together, these data indicate that ADF and CFL1 contribute to the enrichment of free barbed ends that are detected at row 2 stereocilia tips.

Since ADF and CFL1 regulate actin in stereocilia, we next sought to determine if actin severing impacts stereocilia morphology by analyzing IHCs from *Adf*$^{-/-}$ *Cfl1*$^{fl/+}$ *Atoh1-cre*

mice. Analysis was complicated because stereocilia bundle architecture was often disrupted and stereocilia dysmorphology differed widely (Figure S4A), perhaps because of variable developmental timing of *Atoh1-cre* mediated knockout between cells. When analysis was restricted to bundles with the most normal morphology, the widths of IHC stereocilia in row 3 increased by 23% and in protrusions medial to row 3 (indicated as row 4+) widths increased by 20%. In contrast, row 1 and row 2 widths were unchanged ($p = 0.22$ and 0.87, respectively) (Figure S4B–C). Correspondingly, F-actin labeled medial protrusions were more evident in P6 $Adf^{-/-}$ $Cfl1^{fl/+}$ *Atoh1-cre* IHCs than in control cells, suggesting ADF/CFL1 normally contributes to disassembling these structures (Figure S4D).

To assess stereocilia morphology while bypassing the most severe developmental defects such as disrupted bundle polarity, we induced *Cfl1* knockout using the ubiquitously expressed, tamoxifen induced *Cagg-creER* transgene in $Adf^{-/-}$ mice ($Adf^{-/-}$ $Cfl1^{fl/fl}$ *Cagg-creER*). Tamoxifen was administered at P2 to produce an induced double knockout (iDKO) and stereocilia were analyzed at P5 because mice failed to survive past this timepoint. ADF/CFL1 immunostaining was markedly reduced in some iDKO cells but retained in others (Figure S5). Compared to $Adf^{+/-}$ $Cfl^{fl/fl}$ (control) IHCs, many iDKO row 3 stereocilia often had abnormally tapered extensions, while row 2 tips appeared largely unaffected (Figure 7A). OHC stereocilia tips also appeared to be morphologically unaffected (Figure 7B). The lengths of IHC row 1 and row 2 stereocilia were approximated from confocal stacks that were digitally resliced to show the z-dimension (Figure 7C). Row 2 stereocilia lengths were unchanged even though ADF/CFL1 localization is most evident at their tips. In contrast, iDKO IHC row 1 stereocilia were shorter than those in control bundles. Despite the changes in row 1 length, immunostaining showed that EPS8 remained similarly enriched at the tips of row 1 iDKO stereocilia (Figure 7D), suggesting that loss of ADF/CFL1 did not lead to dramatic changes in row-specific protein localization. Finally, stereocilia widths measured from SEM micrographs were also affected, being increased in IHC row 3 and in all rows of OHC bundles from iDKO mice (Figure 7E). Although changes in dimension do not correlate well with the availability of actin barbed ends, ADF and CFL1 are required for normal bundle patterning and stereocilia morphogenesis.

DISCUSSION:

We found that mechanotransduction promotes the recruitment and activation of the actin severing proteins ADF and CFL1 at the tips of mechanotransducing stereocilia, where these proteins remodel actin to increase the availability of filament barbed ends. ADF/CFL1 localization depends on proper establishment of row identity, which in turn depends on the MYO15/EPS8 complex and mechanotransduction onset. However, acutely blocking mechanotransduction after row identity was established also resulted in a reduction of available barbed ends from row 2 and 3 stereocilia, demonstrating continuous requirement for mechanotransduction to regulate actin.

ADF and CFL1 are well-known to sever actin filaments, but it is less clear how this biochemical activity results in the effects we observed in mutant hair cells, which included decreased levels of available barbed ends, hair bundle malformation, decreased IHC row 1 length, and increased stereocilia width. Mechanisms for each effect can be envisioned, but

it is possible that changes to the cellular actin pool, primarily an increase in F-actin and a decrease in G-actin, contributes to most phenotypes. For example, a large increase in F-actin within the cuticular plate, which is evident in the iDKO cells (Figure 7C) may eventually push the bundle into unusual shapes (Figure S3, S4A). In addition, if most actin is trapped in the filamentous form, then row 1 may not be able to grow at the normal rate because the monomeric actin concentration is too low to support rapid filament elongation.

While row 1 elongation may be an indirect consequence of G-actin concentration, the effects of ADF/CFL1 on stereocilia width and barbed end availability seem to require a more direct mechanism such as changing the way actin filaments are packed in the core or changing the number of filaments that are added to the core. To decrease width, severing could rapidly destabilize actin filaments, which has been observed in cellular and biochemical contexts when CFL1 is combined with coronin, and AIP1 [48, 49]. Coronin localizes to stereocilia and stereocilia morphology is not maintained in AIP1 mutants [15, 50], suggesting this is a plausible mechanism. Concurrently, severing may regulate barbed end availability by removing filament ends that are bound by capping proteins like CAPZ, TWF2, and EPS8 [51]. The fate of the newly uncapped filament would depend on context and could elongate under conditions that favor polymerization or shorten if, for example, it is rapidly recapped. In any case, the balance of capping is clearly a factor in stereocilia morphogenesis as overexpression of CAPZ or TWF2 affects stereocilia length and width [35, 36]. Overall, the effect of ADF/CFL1 on stereocilia width likely depends on where severing occurs along the protrusion and what other proteins are present at the same time.

Removing the capped filament ends is also a potential mechanism for how ADF and CFL1 might control barbed end availability at mechanotransducing stereocilia tips. Perhaps this sort of activity can shape the core as loss of ADF/CFL1 resulted in abnormally tapered tips in IHC row 3 stereocilia. However, neither the shape of iDKO IHC row 2 stereocilia or OHC stereocilia tips was affected, nor was the length of IHC row 2 stereocilia. Thus, it seems that barbed end availability at stereocilia tips is not necessarily critical for regulating the morphology of mechanotransducing stereocilia. Therefore, ADF/CFL1 may regulate stereocilia actin through another mechanism or at a different location within stereocilia.

If the role of actin severing is not exclusively to shape the stereocilia actin core, then a more complicated model of actin regulation at stereocilia tips may be required. Besides severing, other activities such as capping and nucleation will also influence barbed end availability. No actin nucleating proteins have been identified at stereocilia tips, but capping proteins are certainly present. TWF2, shown to both cap barbed ends and promote barbed end depolymerization [33, 52], localizes to mechanotransducing stereocilia tips from at least P7 [35, 36]. As hair cells mature, CAPZ, which is well-known to cap actin barbed ends [32], also becomes clearly evident at mechanotransducing stereocilia tips [35]. If ADF and CFL1 simply antagonize capping proteins by severing filaments, then it seems unlikely all of these proteins would selectively localize at the tips of the same stereocilia. Interestingly, actin, CAPZ, CFL1 and a nucleator are sufficient to reconstitute in vitro bead motility [53]. Perhaps colocalization of capping and severing proteins indicates an actin network apart from that comprising the stereocilia core.

The enrichment of available actin filament ends at row 2 stereocilia tips depends on mechanotransduction. This relationship could be direct if, for example, an adaptor protein links ADF/CFL1 to the mechanotransduction channel or a Ca^{2+}-sensitive signaling cascade activates ADF/CFL1. However, mechanotransduction is likely not sufficient to drive actin regulation as available barbed ends are reduced in IHCs of *Myo15* mutants, which retain resting mechanotransduction currents at P3+4DIV [54]. Instead, establishing normal stereocilia row identity, which depends on both the MYO15 complex and mechanotransduction [24, 25], is likely a prerequisite for enriching ADF/CFL1 at row 2/3 stereocilia tips.

Once normal row identity is established, mechanotransduction activity is still required to regulate ADF/CFL1 localization and activity. After some developmental point inhibiting mechanotransduction does not seem to result in a shift of row 1 proteins to row 2 tips. However, mechanotransduction is still required to maintain mechanotransducing stereocilia as shown by studies where blocking mechanotransduction in culture or deleting tip link components *in vivo* results in shortening and eventual loss of mechanotransducing stereocilia while row 1 stereocilia remain intact [29–31, 55]. Correspondingly, we found that blocking mechanotransduction decreased the availability of actin barbed ends at row 2 stereocilia tips, suggesting this mechanotransduction is required to maintain the localization and activity of barbed end regulators like ADF/CFL1.

The mechanisms that couple mechanotransduction to actin remodeling are likely important for both the development and maintenance of stereocilia. In addition, mechanotransduction may tune actin networks that could have other roles at mechanotransducing stereocilia tips, for example to modulate cortical stiffness for optimal channel activity. We found that ADF and CFL1 link mechanotransduction to actin remodeling, which is reflected in an increase in the availability of filament barbed ends. This is a defining feature of the properly differentiated mechanotransducing stereocilia that is required for auditory function.

STAR METHODS

RESOURCE AVAILABILITY

Lead Contact—For resources and reagents or more information on the material in this publication, please coordinate with the Lead Contact, Benjamin Perrin (bperrin@iupui.edu).

Materials Availability—The *Eps8* mutant lines generated in this study are available upon request.

Data and Code Availability—The datasets generated in this study are available at Figshare.com at https://figshare.com/s/cb3bc135eabf4cc891d5.

EXPERIMENTAL MODEL AND SUBJECT DETAILS

The sexes of the mice used in this study were not determined prior to dissection and were not considered as a variable in our experiments. Determining the sex of mouse pups at early postnatal ages, before the genitalia have fully developed, is difficult without genotyping. Instead, we used both sexes indiscriminately. C57BL/6 (MGI:3028467,

JAX:000664) were used for the measurement of free barbed ends at stereocilia tips over development (Figure 2) and experiments using tubocurarine (Figure 3). Two previously published mouse lines were used to express EGFP-labeled actin and both were maintained on a C57BL/6 background. One mouse line (Figure1A) utilizes β-actin-EGFP that has been incorporated into a FLip flEx (FLEx) vector (C57BL/6-Tg(CAG-tdTomato,Actb/EGFP)1Erv/J, MGI:5810463, JAX:029889). In these mice, tdTomato protein is widely expressed until after cre-mediated recombination of the transgene, when β-actin-EGFP expression replaces tdTomato [15]. The other mouse line (Figure1B) expressed the EGFP-β-actin fusion protein under the control of a *Myo7a* promoter in the *hprt* locus of the X chromosome (Myo7a::EGFP-β-actin or C3;129S7-Hprttm2Brd/Biat, MGI:5561057) [14], which in the cochlea is primarily expressed in IHCs [56]. The *Eps8* mutant mouse lines were generated using CRISPR-Cas9 introduced to C57BL/6 embryos via the Improved Genome-Editing via Oviductal Nucleic Acid Delivery (i-GONAD) method [57, 58]. An RNA complex of crRNA (TGACCACCTTCGTGCTGGATCGG, targeting *Eps8* or ACGGTCATCCACCCCTTGAAGG targeting the Tyrosinase (*Tyr*) gene) and tracrRNA (IDT, Cat.# 1072534) was formed by mixing equal amounts of each RNA, which were resuspended in duplex buffer (IDT, Cat.# 11–01-03–01) at 100 μM, heating to 94°C for 5 minutes and cooling to room temperature on the bench top. The guide complex was assembled with Recombinant *S. pyogenes* Cas9 nuclease (IDT, Cat.# 1081058) by mixing 2.5 μL of *Eps8* guide complex, 2 μL *Tyr* complex (included to aid in identifying targeted mice because Tyrosinase is required for pigment formation), 1.5 μL of 100μg/mL Cas9, 9 μL of PBS and incubating at room temperature for 10 min. Fast Green (0.5 μL of a 1% filter sterilized solution) (Thermo Fisher Scientific, Cat.# BP123–10) was added to aid visualization. C57BL/6 mice were mated, and females with copulation plugs were identified the next morning. These females were used the same afternoon (13–16 h post-coitum) for the i-GONAD procedure. Mice were anesthetized with isoflurane, the oviducts were exposed via an incision on the back of the mouse, and each oviduct was filled with the guide RNA:Cas9 complex by injecting with a needle pulled from a glass capillary. The oviduct was then electroporated with square wave pulses (8 pulses, duration 5 ms, interval 1 s, field intensity 50 V) delivered via tweezertrodes (BTX, 3mm platinum Cat.# 45–0487) connected to an ECM830 electroporator (BTX, Cat.# 45–0662). The incision was closed with surgical staples. Following normal vaginal delivery, pups bearing mutations in *Eps8* induced by CRISPR-Cas9 were identified by amplifying the targeted region using polymerase chain reaction (PCR) (Primers: 5'-AATACTATGCTGTTGCAGCCCC-3' and 5'-ACCGGTACACTTTGCAAACAAGA-3') and subcloning fragments into pTOPOblunt, which was then transformed into DH5alpha competent cells. Individual colonies were isolated, subjected to PCR using the same primers, and the products were Sanger sequenced to identify mutations. Two mutations were identified as indicated in Figure S3. These mice were backcrossed to C57BL/6 and then intercrossed to generate either homozygous or compound mutants. *Myo15*$^{sh2/sh2}$ (*Myo15*^{sh2}, MGI:1857036, RRID:IMSR_JAX:000109), *Tmie*$^{-/-}$ (*Tmie*^{tm2Mull}, MGI:5784557), *Atoh1-cre* (Tg(Atoh1-cre)1Bfri, MGI:3775845, RRID:IMSR_JAX:011104), and *Cagg-creER* (Tg(CAG-cre/Esr1*)5Amc, MGI:2182767, RRID:IMSR_JAX:017595) mouse lines have been previously described [47, 59–63]. The *Adf*$^{-/-}$ (Dstn^{corn1}, MGI:3817225, RRID:MGI:3817225) mice were a kind gift from the Ikeda lab (University of Wisconsin-Madison) and *Cfl1*$^{fl/fl}$ (Cfl1$^{tm1.1Wit}$, MGI:4943295,

RRID:MGI:4943295) mice were graciously provided by Walter Witke and Christine Gurniak (University of Bonn). All mutant lines were backcrossed and maintained on a C57BL/6 background. Animals were maintained using standard husbandry and housing practices. All animal experiments were reviewed and approved by the Institutional Animal Care and Use Committees of Indiana University – Purdue University, Indiana University School of Medicine, and NIH-NIDCD.

METHOD DETAILS

Imaging by fluorescence microscopy—The cochlear shell was removed from the temporal bone and placed in phosphate-buffered saline (PBS). The bony cartilage, the lateral wall, Reissner's membrane, and the cochlear nervous tissue were removed prior to fixation. Dissected tissue was fixed in 4% paraformaldehyde (PFA) (Electron Microscopy Sciences, Cat.# 15710) in PBS for 16–18 h at 4°C. The tectorial membrane was removed after fixation to expose the reticular lamina of the sensory epithelium, where the stereocilia bundles are located. To label ADF and CFL1 in C57BL/6 mice, the middle turn was dissected from 3 or more mice at P0, P1, P2, P6, and P26. After PFA fixation, these samples were placed in 100% methanol for 10 min at −20°C, followed by permeabilization with 0.5% Triton X-100 (Sigma, Cat.# X-100–100ML) in PBS for 10 min at room temperature, and blocked with 5% goat serum in PBS for 2 h at room temperature or 16–18 h at 4°C. Samples were then immunolabeled with 1:100 dilution of anti-CFL1 rabbit monoclonal antibody (Cell Signaling Technology, RRID:AB_10622000, Cat.# 5175), which labels both ADF and CFL1, and 1:400 dilution of anti-β-actin mouse monoclonal antibody conjugated to FITC dye (Abcam, RRID:AB_305394, Cat.# ab6277) in 5% goat serum for 1 h. In samples which were not treated with methanol, F-actin was stained with 1:400 phalloidin labeled with Alexa-488 (Invitrogen, Cat.# A12379) in 5% goat serum. To label EPS8 in *Myo15*$^{sh2/+}$, *Myo15*$^{sh2/sh2}$, *Eps8*$^{-/+}$, and *Eps8*$^{-/-}$ mice, anti-EPS8 mouse antibody (BD Biosciences, RRID:AB_397544, Cat.# 610143) was used at 1:100 dilution in 5% goat serum and incubated with the tissue for 1 h. Immunolabeling with mouse anti-Flag (Sigma Aldrich, Cat.# F3165, RRID:AB_259529) and mouse anti-His conjugated to iFluor488 (GenScript, Cat.# A01800) was performed in P5 or P6 C57BL/6 tissue which was first permeabilized with 0.05% Saponin extract (Sigma Aldrich, Cat.# S4521) in cytoskeletal stabilization buffer (see Probing barbed end availability in Method Details) and then fixed with 4% PFA in PBS for 30 min to 2 h. All unlabeled primary antibodies were detected using either Alexa-488 (Invitrogen, RRID:AB_138404, Cat.# A11029), Alexa-546 (Invitrogen, RRID:AB_143051, Cat.# A11035), Alexa-568 (Invitrogen, RRID:AB_10563566, Cat.# A11036), or Alexa-647 (Invitrogen, RRID:AB_141725, Cat.# A21236) goat secondary antibodies. Samples were mounted in Prolong Diamond (Thermo Fisher Scientific, Cat.# P36961), cured overnight in the dark, and imaged with a Leica Plan Apo 63x/1.40 NA oil immersion objective on Leica SP8 inverted confocal microscope (Leica Microsystems, RRID:SCR_018169) operating in resonant mode. Images were captured using Leica Application Suite X (Leica Microsystem, RRID:SCR_013673) and deconvolved using Leica LIGHTNING deconvolution with the recommended settings. ImageJ (NIH, RRID:SCR_002285) and Adobe Illustrator software (Adobe, RRID:SCR_010279) were used to generate figures. Airyscan images were acquired on a Zeiss Airyscan LSM 880 system (Carl Zeiss Microscopy LLC, Germany) in the super-resolution Airyscan mode using the multichannel frame scan mode and a 63x/1.40

NA oil immersion DIC M27 objective. The Airyscan processing algorithm running in auto mode was applied to obtain the final images using Zeiss Zen Black software v2.3 SP1 FP3, 64-bit (Carl Zeiss Microscopy LLC, Germany). The green and red fluorescence signal were acquired using a 488 nm argon laser at 0.1% laser power and a 561 nm diode pumped solid state laser at 0.05% power, correspondingly. All czi format images obtained with Zen software were exported as TIF images, and Adobe Photoshop software (RRID:SCR_014199) was used to crop the images and/or uniformly adjust brightness.

Fluorescence recovery after photobleaching (FRAP)—C57BL/6 mouse cochlea were dissected at P3 or P4 and cultured in DMEM/F12 (Thermo Fisher Scientific, Cat.# 11039047) on the lids of 60×15 mm tissue culture treated dishes (USA Scientific Cat.# CC7672–3359). After incubating at 37°C and 5% CO_2 for 30 min to 4 h, explants were prepared for imaging by placing a 25 mm glass coverslip (Fisherbrand, Cat.# 12–545-102 25CIR) over top of a ring of silicone grease surrounding the sample, forming a sealed chamber containing a small volume of media. The remaining media was removed, and the chamber inverted over a Leica HC PL APO 40x/1.10 W motCORR CS2 water immersion objective on a Leica SP8 confocal microscope equipped with an Okolab microscope incubator that was preheated to and maintained at 37°C during imaging experiments. Samples were imaged in resonant mode using the Leica FRAP module. IHC stereocilia were imaged using a 488 nm argon laser at 1–2% power. Regions of interest (ROIs) were bleached using the same laser operating at 100% laser power. Post-bleached samples were imaged using a HyD (hybrid) detector and images were deconvolved using Leica LIGHTNING deconvolution recommended settings. All images were captured using the XYZt format which provided 3D stack of the sample at each timepoint during the experiment. Fluorescence intensities at row 1 or row 2 tips were quantified as described in the “Quantification and Statistical Analysis” section.

Probing barbed end availability—Samples were dissected in Hank’s Balanced Salt Solution (HBSS, Life Technologies, Cat.# 14025092) to remove the lateral wall, Reissner’s membrane, and tectorial membrane prior to permeabilization. After dissection, live tissue was incubated in cytoskeletal buffer (20 mM HEPES, pH 7.5, 138 mM KCl, 4 mM $MgCl_2$, 3 mM EGTA, 1% bovine serum albumin containing 0.05% Saponin to permeabilize the cells, as well as 2 mM fresh ATP (Sigma Aldrich, Cat.# 10127531001) and 1 μM rhodamine-labeled rabbit skeletal G-actin (Cytoskeleton, Inc., Cat.# AR05) to label actin incorporation sites. Samples were incubated in this solution for 5 min at room temperature. For His-CAPZ and Flag-FSCN1 (described below) experiments, 100 nM and 11 μM of the purified protein, respectively, were used in place of rhodamine-labeled actin. Samples were washed with cytoskeletal buffer and fixed with 4% PFA for 30 min to 2 h at room temperature. F-actin was stained with 1:400 phalloidin conjugated to Alexa-488 (Thermo Fisher Scientific, Cat.# A12379) and imaged as described in the “Imaging by fluorescence microscopy” section. To examine the barbed ends of filaments in the actin core of auditory stereocilia, the middle turn was dissected and rhodamine-actin incorporation was localized at P0, P1, P2, P6 using cochlear tissue from 3 or more mice at each timepoint. Two or more images were taken from each cochlea and both cochleae were imaged for each mouse. Fluorescence intensities at row

1 or row 2 tips were quantified as described in the “Quantification and Statistical Analysis” section.

Expression and Purification of His-CAPZ and Flag-FSCN1—The expression construct for capping protein (mouse CAPZβ and 6XHis-tagged CAPZα1) was a gift from Antoine Jégou & Guillaume Romet-Lemonne (Addgene Plasmid# 89950, http://n2t.net/addgene:89950, RRID:Addgene_89950) [64]. Competent *Escherichia Coli* BL21 (DE3) cells were transformed with His-CAPZα1/β plasmid. Successful transformants were selected by incubating bacteria at 37°C on LB agar plates containing ampicillin. A single colony was used to inoculate 100 mL LB-ampicillin starter culture which was grown overnight at 37°C. The overnight culture was used to inoculate 2 L of autoinduction media (each liter contained at final concentrations: 90 mM KPi, pH 7.0, 1 g/L glucose, 2 g/L lactose, 0.5 % glycerol, 12 g peptone, and 24 g yeast extract), supplemented with ampicillin (50 μg/mL final). The cells were grown at room temperature for 48 hours after which they were harvested by centrifugation. The cell pellet was re-suspended in 100 mL lysis buffer (25 mM HEPES pH 7.5, 300 mM NaCl, 10% glycerol, 1 mM β-mercaptoethanol, 30 mM Imidazole, and 0.5 mM PMSF). The re-suspended cells were then lysed by sonication. The cell lysate was then centrifuged to remove cellular debris and the cleared lysate was loaded onto a Ni-NTA column, which was pre-equilibrated with Ni-Wash buffer (25 mM HEPES pH 7.5, 300 mM NaCl, 10% glycerol, and 10 mM imidazole). After washing the column with 10 CV of Ni-Wash buffer, the recombinant His-CAPZα1/β protein was eluted with 100 mL of a linear gradient of 10–300 mM imidazole in Ni-Elution buffer (25 mM HEPES pH 7.5, 300 mM NaCl, 10% glycerol and 300 mM imidazole. The purity of the CAPZ containing fractions was assessed by SDS-PAGE. The fractions containing over 95% pure CAPZ were pooled together and dialyzed overnight against His-CAPZα1/β storage buffer (25 mM HEPES pH 7.5, 300 mM NaCl, and 10% glycerol). The concentration of the dialyzed protein was measured and aliquoted. A human *Fscn1* cDNA clone (a kind gift from Steve Almo, [65]) was amplified by PCR with primers to add an N-terminal Flag-tag and cloned into pENTR/D-TOPO (Thermo Fisher Scientific) following the manufacturer’s instructions. The Flag-tagged construct was shuttled to pDEST8 (Thermo Fisher Scientific) for expression in insect cells. The pDEST8 construct was transformed into DH10bac *Escherichia coli* (Thermo Fisher Scientific) to produce the recombinant bacmid, which was purified and used to transfect SF21 cells cultured in SF900 III media (Thermo Fisher Scientific, Cat.# 12658019). After viral amplification, infected cell pellets were lysed in PBS with protease inhibitors by sonication and centrifuged at 20,000 × *g*. Flag-FSCN1 protein was purified from the lysate by Flag-affinity chromatography using Flag-antibody-conjugated beads (Sigma Aldrich), eluted with Flag peptide, dialyzed into PBS, and centrifuged at 100,000 × *g* for 30 min with soluble protein collected from the supernatant. The concentration was measured by A_{280}.

Channel block with tubocurarine—The organ of Corti was dissected from C57BL/6 mice in DMEM/F12 at room temperature and the bony capsule and spiral ligament were removed. A 0.20 mm stainless steel Minutien pin (Fine Science Tools, Cat.# 26002–20) was placed through the modiolus to skewer the explant and hold it suspended in the media. The tip of the minutien pin coming out from the bottom of the modiolus, near

the basal turn, was then embedded in a layer of Sylgard 184 (Electron Microscopy Sciences, Cat.# 24236–10) at the bottom of a 35×10mm culture dish (USA scientific, Cat.# CC7682–3340) or a 24-well culture plate (Thermo Fisher Scientific, Cat.# 08–772-1). Explants were incubated at 37°C and 5% CO_2 in media containing 111 μg/mL sodium pyruvate (Thermo Fisher Scientific, Cat.# BP356–100), 111 μg/mL penicillin G (Sigma Aldrich, Cat.# P3032–10MU), 22 ng/mL human epidermal growth factor (Sigma Aldrich, Cat.# E9644–0.2MG), 11 ng/mL fibroblast growth factor-basic (Sigma Aldrich, Cat.# F0291–25UG), 55 ng/mL insulin-like growth factor-1 (Sigma Aldrich, Cat.# I8779–50UG), 55 ng/mL heparin sulfate proteoglycan (Sigma Aldrich, Cat.# H4777–0.1MG), 1X N-2 Supplement (Sigma Aldrich, Cat.# 17504048) and 1X B-27 supplement (Thermo Fisher Scientific, Cat.# 17504044). Additionally, deionized water or 100 μM tubocurarine hydrochloride pentahydrate (Sigma Aldrich, Cat.# T2379) were added to control and treated explant media, respectively. After incubation for 6, 18, and 48 h, the tectorial membrane and modiolus were removed in the culture media and further processed for either rhodamine-actin incorporation or EPS8 staining. Explants used to label EPS8 after tubocurarine channel block and those used to examine rhodamine-actin incorporations were cultured concurrently at all timepoints and the same number of samples were used for both experiments.

Scanning electron microscopy (SEM)—To prepare samples for SEM, dissected tissue was fixed in 2.5% glutaraldehyde, 0.1 M sodium cacodylate (Electron Microscopy Sciences, Cat.# 16537–15) supplemented with 2 mM $CaCl_2$ for 4 h at room temperature or 16–18 h at 4°C. To reduce surface charging, the tissue was incubated in 2% each of arginine, glutamine, glycine, and sucrose in water for 16–18 h, then in 2% tannic acid (Electron Microscopy Sciences, Cat.# 21710) and guanidine hydrochloride in water for 2 h, followed by incubation in 1% OsO_4 (Electron Microscopy Sciences, Cat.# 19152) in water for 1 h. Samples were washed three times with water in between solutions. The samples were afterward gradually transitioned to 100% ethanol, then transitioned to CO_2 and desiccated using a Samdri-780 critical point dryer (Tousimis Research Corporation). Samples were sputter coated with gold before imaging with a JEOL JSM-7800F Schottky field emission scanning electron microscope (JEOL). Widths of stereocilia were measured at the widest region along the length of the stereocilium using ImageJ software. Tips of row 3 inner hair cell stereocilia were pseudo-colored yellow using Adobe Photoshop software

QUANTIFICATION AND STATISTICAL ANALYSIS

Data management—Normalization and averaging of datasets were done in Microsoft Excel (Version 16.41). Data tables were assembled to pool the data for a given experiment and calculations were done within the data table. A PivotTable analysis was performed and used to stage the data for export to Prism 8 software (GraphPad, RRID:SCR_002798). Descriptive and statistical analyses were performed in Prism 8.

FRAP quantification—For FRAP analysis in Figure 1C, regions of interest (ROIs) encompassing the tips of either row 1 or row 2 were established and measured for each bundle. Intensity values were normalized to the unbleached portion of the same or another bundle within the same image. Values were then normalized to the maximum value of row 2 within the bundle to allow for comparisons between cells. Average normalized intensity was

plotted against time and a one-phase decay curve was fitted using a least squares regression in Prism 8 software. Datapoints in the graph of Figure 1C represent the mean ± SD.

Rhodamine-actin and EPS8 labeling quantification—Fluorescence intensity at stereocilia tips was measured using a ~0.1 μm^2 circle at the brightest z-slice in the image stack. In Figure 2F, tip intensities were normalized to the average tip intensities of row 2 within the same image to control for imaging depth and labeling variability between samples. This allowed for a comparison between IHC and OHC rhodamine-actin incorporation. In Figure 2G, the data in Figure 2F was normalized to the cross-sectional area, which was determined by the average stereocilia widths measured from scanning electron micrographs of P5 *Adf*$^{+/-}$ *Cfl1*$^{fl/fl}$ control IHCs and OHCs (Figure 7E). Details about how widths were measured can be found in the subsection of "Quantification and Statistical Analysis" describing width measurements. Rhodamine-actin incorporation in Figure 3C, 5D, and 6D (left graph) was measured and analyzed as described for Figure 2F, excluding the quantification of row 3 tip intensities. Only bundles with discernable rows were included in the analysis of rhodamine-actin incorporation while severely dysmorphic bundles frequently seen in the *Adf*$^{-/-}$ *Cfl1*$^{fl/+}$ *Atoh1-cre* mutants were excluded. EPS8 tip labeling intensities were measured in the same manner as rhodamine-actin incorporation. (Figure 3G, 7D and Figure S1D and 1G). To quantify the enrichment of proteins to either row 1 or 2 stereocilia tips (Figure 3F, 3G, and 6D), the average tip intensity of one row was divided by the average intensity of the other row.

Stereocilia length quantification—To compare row 1 and row 2 stereocilia lengths (Figure 7C), stacks of immunofluorescence images were digitally resliced using the Reslice tool in ImageJ. Stacks were digitally resliced with interpolation before measuring stereocilia in the x,z image. The line measurement tool in ImageJ was used to obtain the mean grey value for the actin core. The tip of a stereocilium was identified as the pixel closest to 50% the mean grey value of the actin core. The 50% cut-off value was chosen to make estimates more consistent and to remove biases. The base was determined by the apparent insertion point into the cuticular plate. In the resliced images, the top of the cuticular plate is readily identifiable by phalloidin staining within the actin network and its absence outside of the network (Figure 7C). To estimate stereocilia length, the distance between the tip and the base of the stereocilium was calculated using a three-dimension line equation.

Stereocilia width quantification—Measurements of stereocilia widths (Figure 7E and Figure S4C) were acquired using scanning electron micrographs of stereocilia bundles with approximately perpendicular orientation. The widest visible point along the stereocilium shaft was measured to reduce the possibility of measuring a tapered stereocilia tip, which are prevalent at the ages examined. If there was ambiguity as to whether it was the tip or shaft, that stereocilia was not measured. A line was drawn perpendicularly across the stereocilium shaft and the length of this line is measured. This was done for all measurable stereocilia in the properly oriented half of the bundle. As was done with measurements of rhodamine-actin incorporation, only bundles with discernable rows were included in the analysis of stereocilia widths while the severely dysmorphic bundles seen in the *Adf*$^{-/-}$ *Cfl1*$^{fl/+}$ *Atoh1-cre* mutants were not measured.

Statistical analysis—Figure 3C, 5D, 6D (left graph), 7C–E, and figure S4C: A one-way ANOVA with Tukey's multiple comparisons test was used to determine significance using a 0.05 alpha value.

Figure 3F–G, 6D (right graph), and figure S1C–D and 1G: A Student's t-test (unpaired, two-tailed) was used to compare the enrichment ratios between control and experimental conditions.

Supplementary Material

Refer to Web version on PubMed Central for supplementary material.

ACKNOWLEDGEMENTS:

Funding was provided by the intramural research program of the NIH, NIDCD, DC000039 to TBF and by the NIDCD grant R01DC015495 to BJP.

REFERENCES

1. Tilney LG, Derosier DJ, and Mulroy MJ (1980). The organization of actin filaments in the stereocilia of cochlear hair cells. J Cell Biol 86, 244–259. [PubMed: 6893452]
2. Kazmierczak P, Sakaguchi H, Tokita J, Wilson-Kubalek EM, Milligan RA, Muller U, and Kachar B. (2007). Cadherin 23 and protocadherin 15 interact to form tip-link filaments in sensory hair cells. Nature 449, 87–91. [PubMed: 17805295]
3. Beurg M, Fettiplace R, Nam JH, and Ricci AJ (2009). Localization of inner hair cell mechanotransducer channels using high-speed calcium imaging. Nat Neurosci 12, 553–558. [PubMed: 19330002]
4. Schwander M, Kachar B, and Muller U. (2010). Review series: The cell biology of hearing. J Cell Biol 190, 9–20. [PubMed: 20624897]
5. Flock A, and Cheung HC (1977). Actin filaments in sensory hairs of inner ear receptor cells. J Cell Biol 75, 339–343. [PubMed: 318131]
6. Chou SZ, and Pollard TD (2019). Mechanism of actin polymerization revealed by cryo-EM structures of actin filaments with three different bound nucleotides. Proc Natl Acad Sci U S A 116, 4265–4274. [PubMed: 30760599]
7. Fujiwara I, Vavylonis D, and Pollard TD (2007). Polymerization kinetics of ADP- and ADP-Pi-actin determined by fluorescence microscopy. Proc Natl Acad Sci U S A 104, 8827–8832. [PubMed: 17517656]
8. Pollard TD (1986). Rate constants for the reactions of ATP- and ADP-actin with the ends of actin filaments. J Cell Biol 103, 2747–2754. [PubMed: 3793756]
9. Wegner A, and Isenberg G. (1983). 12-fold difference between the critical monomer concentrations of the two ends of actin filaments in physiological salt conditions. Proc Natl Acad Sci U S A 80, 4922–4925. [PubMed: 6576365]
10. Meenderink LM, Gaeta IM, Postema MM, Cencer CS, Chinowsky CR, Krystofiak ES, Millis BA, and Tyska MJ (2019). Actin Dynamics Drive Microvillar Motility and Clustering during Brush Border Assembly. Dev Cell 50, 545–556 e544. [PubMed: 31378589]
11. Pollard TD, and Borisy GG (2003). Cellular motility driven by assembly and disassembly of actin filaments. Cell 112, 453–465. [PubMed: 12600310]
12. Tyska MJ, and Mooseker MS (2002). MYO1A (brush border myosin I) dynamics in the brush border of LLC-PK1-CL4 cells. Biophys J 82, 1869–1883. [PubMed: 11916846]
13. Zheng L, Beeler DM, and Bartles JR (2015). Characterization and regulation of an additional actin-filament-binding site in large isoforms of the stereocilia actin-bundling protein espin. Journal of Cell Science 128, 2208–2208. [PubMed: 26034062]

14. Zhang DS, Piazza V, Perrin BJ, Rzadzinska AK, Poczatek JC, Wang M, Prosser HM, Ervasti JM, Corey DP, and Lechene CP (2012). Multi-isotope imaging mass spectrometry reveals slow protein turnover in hair-cell stereocilia. Nature 481, 520–524. [PubMed: 22246323]
15. Narayanan P, Chatterton P, Ikeda A, Ikeda S, Corey DP, Ervasti JM, and Perrin BJ (2015). Length regulation of mechanosensitive stereocilia depends on very slow actin dynamics and filament-severing proteins. Nat Commun 6, 6855. [PubMed: 25897778]
16. Drummond MC, Barzik M, Bird JE, Zhang DS, Lechene CP, Corey DP, Cunningham LL, and Friedman TB (2015). Live-cell imaging of actin dynamics reveals mechanisms of stereocilia length regulation in the inner ear. Nat Commun 6, 6873. [PubMed: 25898120]
17. Belyantseva IA, Boger ET, and Friedman TB (2003). Myosin XVa localizes to the tips of inner ear sensory cell stereocilia and is essential for staircase formation of the hair bundle. Proc Natl Acad Sci U S A 100, 13958–13963. [PubMed: 14610277]
18. Delprat B, Michel V, Goodyear R, Yamasaki Y, Michalski N, El-Amraoui A, Perfettini I, Legrain P, Richardson G, Hardelin JP, et al. (2005). Myosin XVa and whirlin, two deafness gene products required for hair bundle growth, are located at the stereocilia tips and interact directly. Hum Mol Genet 14, 401–410. [PubMed: 15590698]
19. Holme RH, Kiernan BW, Brown SD, and Steel KP (2002). Elongation of hair cell stereocilia is defective in the mouse mutant whirler. J Comp Neurol 450, 94–102. [PubMed: 12124769]
20. Manor U, Disanza A, Grati M, Andrade L, Lin H, Di Fiore PP, Scita G, and Kachar B. (2011). Regulation of stereocilia length by myosin XVa and whirlin depends on the actin-regulatory protein Eps8. Curr Biol 21, 167–172. [PubMed: 21236676]
21. Mauriac SA, Hien YE, Bird JE, Carvalho SD, Peyroutou R, Lee SC, Moreau MM, Blanc JM, Geyser A, Medina C, et al. (2017). Defective Gpsm2/Galphai3 signalling disrupts stereocilia development and growth cone actin dynamics in Chudley-McCullough syndrome. Nat Commun 8, 14907. [PubMed: 28387217]
22. Tarchini B, Tadenev AL, Devanney N, and Cayouette M. (2016). A link between planar polarity and staircase-like bundle architecture in hair cells. Development 143, 3926–3932. [PubMed: 27660326]
23. Furness DN, Johnson SL, Manor U, Ruttiger L, Tocchetti A, Offenhauser N, Olt J, Goodyear RJ, Vijayakumar S, Dai Y, et al. (2013). Progressive hearing loss and gradual deterioration of sensory hair bundles in the ears of mice lacking the actin-binding protein Eps8L2. Proc Natl Acad Sci U S A 110, 13898–13903. [PubMed: 23918390]
24. Krey JF, Chatterjee P, Dumont RA, O'Sullivan M, Choi D, Bird JE, and Barr-Gillespie PG (2020). Mechanotransduction-Dependent Control of Stereocilia Dimensions and Row Identity in Inner Hair Cells. Curr Biol 30, 442–454 e447. [PubMed: 31902726]
25. Tadenev ALD, Akturk A, Devanney N, Mathur PD, Clark AM, Yang J, and Tarchini B. (2019). GPSM2-GNAI Specifies the Tallest Stereocilia and Defines Hair Bundle Row Identity. Curr Biol 29, 921–934 e924. [PubMed: 30827920]
26. Lelli A, Asai Y, Forge A, Holt JR, and Geleoc GS (2009). Tonotopic gradient in the developmental acquisition of sensory transduction in outer hair cells of the mouse cochlea. J Neurophysiol 101, 2961–2973. [PubMed: 19339464]
27. Waguespack J, Salles FT, Kachar B, and Ricci AJ (2007). Stepwise morphological and functional maturation of mechanotransduction in rat outer hair cells. J Neurosci 27, 13890–13902. [PubMed: 18077701]
28. Beurg M, Cui R, Goldring AC, Ebrahim S, Fettiplace R, and Kachar B. (2018). Variable number of TMC1-dependent mechanotransducer channels underlie tonotopic conductance gradients in the cochlea. Nat Commun 9, 2185. [PubMed: 29872055]
29. Caberlotto E, Michel V, de Monvel JB, and Petit C. (2011). Coupling of the mechanotransduction machinery and F-actin polymerization in the cochlear hair bundles. Bioarchitecture 1, 169–174. [PubMed: 22069509]
30. Caberlotto E, Michel V, Foucher I, Bahloul A, Goodyear RJ, Pepermans E, Michalski N, Perfettini I, Alegria-Prevot O, Chardenoux S, et al. (2011). Usher type 1G protein sans is a critical component of the tip-link complex, a structure controlling actin polymerization in stereocilia. Proc Natl Acad Sci U S A 108, 5825–5830. [PubMed: 21436032]

31. Velez-Ortega AC, Freeman MJ, Indzhykulian AA, Grossheim JM, and Frolenkov GI (2017). Mechanotransduction current is essential for stability of the transducing stereocilia in mammalian auditory hair cells. Elife 6.
32. Caldwell JE, Heiss SG, Mermall V, and Cooper JA (1989). Effects of CapZ, an actin capping protein of muscle, on the polymerization of actin. Biochemistry 28, 8506–8514. [PubMed: 2557904]
33. Helfer E, Nevalainen EM, Naumanen P, Romero S, Didry D, Pantaloni D, Lappalainen P, and Carlier MF (2006). Mammalian twinfilin sequesters ADP-G-actin and caps filament barbed ends: implications in motility. EMBO J 25, 1184–1195. [PubMed: 16511569]
34. Hertzog M, Milanesi F, Hazelwood L, Disanza A, Liu H, Perlade E, Malabarba MG, Pasqualato S, Maiolica A, Confalonieri S, et al. (2010). Molecular basis for the dual function of Eps8 on actin dynamics: bundling and capping. PLoS Biol 8, e1000387.
35. Avenarius MR, Krey JF, Dumont RA, Morgan CP, Benson CB, Vijayakumar S, Cunningham CL, Scheffer DI, Corey DP, Muller U, et al. (2017). Heterodimeric capping protein is required for stereocilia length and width regulation. J Cell Biol 216, 3861–3881. [PubMed: 28899994]
36. Peng AW, Belyantseva IA, Hsu PD, Friedman TB, and Heller S. (2009). Twinfilin 2 regulates actin filament lengths in cochlear stereocilia. J Neurosci 29, 15083–15088. [PubMed: 19955359]
37. Zampini V, Ruttiger L, Johnson SL, Franz C, Furness DN, Waldhaus J, Xiong H, Hackney CM, Holley MC, Offenhauser N, et al. (2011). Eps8 regulates hair bundle length and functional maturation of mammalian auditory hair cells. PLoS Biol 9, e1001048.
38. Bamburg JR (1999). Proteins of the ADF/cofilin family: essential regulators of actin dynamics. Annu Rev Cell Dev Biol 15, 185–230. [PubMed: 10611961]
39. Chan AY, Raft S, Bailly M, Wyckoff JB, Segall JE, and Condeelis JS (1998). EGF stimulates an increase in actin nucleation and filament number at the leading edge of the lamellipod in mammary adenocarcinoma cells. J Cell Sci 111 (Pt 2), 199–211. [PubMed: 9405304]
40. Roy P, and Perrin BJ (2018). The stable actin core of mechanosensory stereocilia features continuous turnover of actin cross-linkers. Mol Biol Cell 29, 1856–1865. [PubMed: 29874122]
41. Perrin BJ, Strandjord DM, Narayanan P, Henderson DM, Johnson KR, and Ervasti JM (2013). beta-Actin and fascin-2 cooperate to maintain stereocilia length. J Neurosci 33, 8114–8121. [PubMed: 23658152]
42. Zhao B, Wu Z, Grillet N, Yan L, Xiong W, Harkins-Perry S, and Muller U. (2014). TMIE is an essential component of the mechanotransduction machinery of cochlear hair cells. Neuron 84, 954–967. [PubMed: 25467981]
43. Wioland H, Guichard B, Senju Y, Myram S, Lappalainen P, Jegou A, and Romet-Lemonne G. (2017). ADF/Cofilin Accelerates Actin Dynamics by Severing Filaments and Promoting Their Depolymerization at Both Ends. Curr Biol 27, 1956–1967 e1957. [PubMed: 28625781]
44. Hadi S, Alexander AJ, Velez-Ortega AC, and Frolenkov GI (2020). Myosin-XVa Controls Both Staircase Architecture and Diameter Gradation of Stereocilia Rows in the Auditory Hair Cell Bundles. J Assoc Res Otolaryngol.
45. Belyantseva IA, Boger ET, Naz S, Frolenkov GI, Sellers JR, Ahmed ZM, Griffith AJ, and Friedman TB (2005). Myosin-XVa is required for tip localization of whirlin and differential elongation of hair-cell stereocilia. Nat Cell Biol 7, 148–156. [PubMed: 15654330]
46. Matei V, Pauley S, Kaing S, Rowitch D, Beisel KW, Morris K, Feng F, Jones K, Lee J, and Fritzsch B. (2005). Smaller inner ear sensory epithelia in Neurog 1 null mice are related to earlier hair cell cycle exit. Dev Dyn 234, 633–650. [PubMed: 16145671]
47. Perrin BJ, Sonnemann KJ, and Ervasti JM (2010). beta-actin and gamma-actin are each dispensable for auditory hair cell development but required for Stereocilia maintenance. PLoS Genet 6, e1001158.
48. Kueh HY, Charras GT, Mitchison TJ, and Brieher WM (2008). Actin disassembly by cofilin, coronin, and Aip1 occurs in bursts and is inhibited by barbed-end cappers. J Cell Biol 182, 341–353. [PubMed: 18663144]
49. Tang VW, Nadkarni AV, and Brieher WM (2020). Catastrophic actin filament bursting by cofilin, Aip1, and coronin. J Biol Chem 295, 13299–13313. [PubMed: 32723865]

50. Lelli A, Michel V, Boutet de Monvel J, Cortese M, Bosch-Grau M, Aghaie A, Perfettini I, Dupont T, Avan P, El-Amraoui A, et al. (2016). Class III myosins shape the auditory hair bundles by limiting microvilli and stereocilia growth. J Cell Biol 212, 231–244. [PubMed: 26754646]
51. Ghosh M, Song X, Mouneimne G, Sidani M, Lawrence DS, and Condeelis JS (2004). Cofilin promotes actin polymerization and defines the direction of cell motility. Science 304, 743–746. [PubMed: 15118165]
52. Hilton DM, Aguilar RM, Johnston AB, and Goode BL (2018). Species-Specific Functions of Twinfilin in Actin Filament Depolymerization. J Mol Biol 430, 3323–3336. [PubMed: 29928893]
53. Loisel TP, Boujemaa R, Pantaloni D, and Carlier MF (1999). Reconstitution of actin-based motility of Listeria and Shigella using pure proteins. Nature 401, 613–616. [PubMed: 10524632]
54. Stepanyan R, and Frolenkov GI (2009). Fast adaptation and Ca2+ sensitivity of the mechanotransducer require myosin-XVa in inner but not outer cochlear hair cells. J Neurosci 29, 4023–4034. [PubMed: 19339598]
55. Corns LF, Johnson SL, Roberts T, Ranatunga KM, Hendry A, Ceriani F, Safieddine S, Steel KP, Forge A, Petit C, et al. (2018). Mechanotransduction is required for establishing and maintaining mature inner hair cells and regulating efferent innervation. Nat Commun 9, 4015. [PubMed: 30275467]
56. Li S, Mecca A, Kim J, Caprara GA, Wagner EL, Du TT, Petrov L, Xu W, Cui R, Rebustini IT, et al. (2020). Myosin-VIIa is expressed in multiple isoforms and essential for tensioning the hair cell mechanotransduction complex. Nat Commun 11, 2066. [PubMed: 32350269]
57. Gurumurthy CB, Sato M, Nakamura A, Inui M, Kawano N, Islam MA, Ogiwara S, Takabayashi S, Matsuyama M, Nakagawa S, et al. (2019). Creation of CRISPR-based germline-genome-engineered mice without ex vivo handling of zygotes by i-GONAD. Nat Protoc 14, 2452–2482. [PubMed: 31341289]
58. Ohtsuka M, and Sato M. (2019). i-GONAD: A method for generating genome-edited animals without ex vivo handling of embryos. Dev Growth Differ 61, 306–315. [PubMed: 31198998]
59. Beyer LA, Odeh H, Probst FJ, Lambert EH, Dolan DF, Camper SA, Kohrman DC, and Raphael Y. (2000). Hair cells in the inner ear of the pirouette and shaker 2 mutant mice. J Neurocytol 29, 227–240. [PubMed: 11276175]
60. Friedman TB, Hinnant JT, Fridell RA, Wilcox ER, Raphael Y, and Camper SA (2000). DFNB3 families and Shaker-2 mice: mutations in an unconventional myosin, myo 15. Adv Otorhinolaryngol 56, 131–144. [PubMed: 10868225]
61. Friedman TB, Liang Y, Weber JL, Hinnant JT, Barber TD, Winata S, Arhya IN, and Asher JH Jr. (1995). A gene for congenital, recessive deafness DFNB3 maps to the pericentromeric region of chromosome 17. Nat Genet 9, 86–91. [PubMed: 7704031]
62. Mitchem KL, Hibbard E, Beyer LA, Bosom K, Dootz GA, Dolan DF, Johnson KR, Raphael Y, and Kohrman DC (2002). Mutation of the novel gene Tmie results in sensory cell defects in the inner ear of spinner, a mouse model of human hearing loss DFNB6. Hum Mol Genet 11, 1887–1898. [PubMed: 12140191]
63. Naz S, Giguere CM, Kohrman DC, Mitchem KL, Riazuddin S, Morell RJ, Ramesh A, Srisailpathy S, Deshmukh D, Riazuddin S, et al. (2002). Mutations in a novel gene, TMIE, are associated with hearing loss linked to the DFNB6 locus. Am J Hum Genet 71, 632–636. [PubMed: 12145746]
64. Shekhar S, Kerleau M, Kuhn S, Pernier J, Romet-Lemonne G, Jegou A, and Carlier MF (2015). Formin and capping protein together embrace the actin filament in a menage a trois. Nat Commun 6, 8730. [PubMed: 26564775]
65. Tseng Y, Fedorov E, McCaffery JM, Almo SC, and Wirtz D. (2001). Micromechanics and ultrastructure of actin filament networks crosslinked by human fascin: a comparison with alpha-actinin. J Mol Biol 310, 351–366. [PubMed: 11428894]

Highlights

- Mechanotransduction regulates actin at the tips of mammalian cochlear stereocilia
- With transduction onset, ADF/cofilin localize to mechanotransducing stereocilia tips
- Actin severing proteins increase available F-actin barbed ends at stereocilia tips
- Normal stereocilia length and width depends on ADF and cofilin-1

McGrath et al. show that ADF/cofilin-1 are recruited to mechanotransducing auditory stereocilia tips, where they increase the availability of F-actin barbed ends. Blocking transduction either by constitutive mutation of the channel or acute inhibition in cochlear explants perturbed ADF/cofilin-1 localization and reduced barbed end availability.

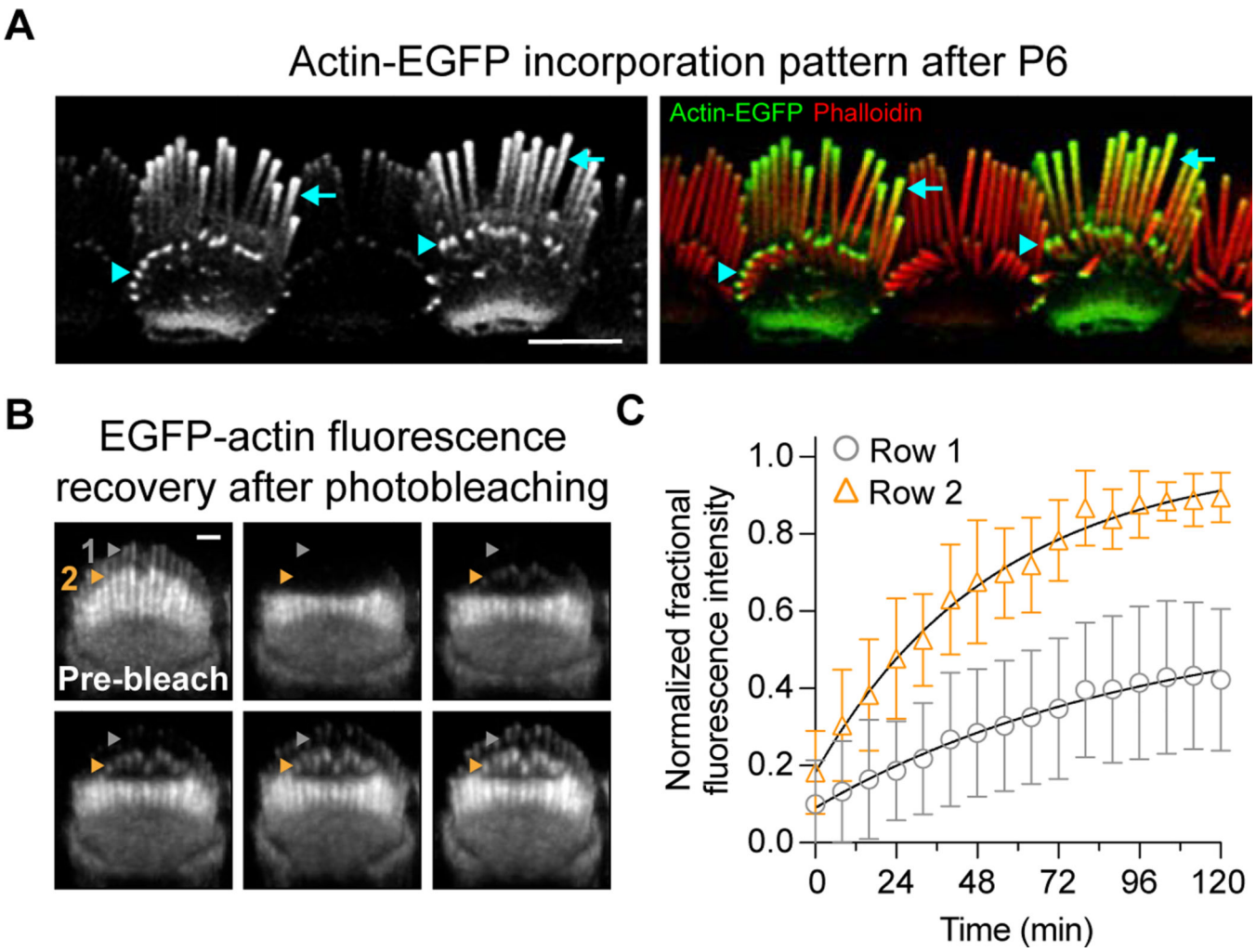

Figure 1. Postnatal actin incorporation patterns.

(A) Actin-EGFP expression was induced at P6 and the organ of Corti was harvested at P28. Actin-EGFP in inner hair cells (IHCs) is shown in grey or green and phalloidin in red. Arrows indicate row 1 stereocilia and arrowheads row 2 stereocilia. Scale bar is 5 μm. (B) Fluorescence recovery after photobleaching of EGFP-actin in P3-P4 IHC stereocilia. Images on the left are maximum intensity projections of an example cell at various timepoints. Grey and orange arrowheads track row 1 and row 2 tips, respectively, through the time series. Scale bar is 1 μm. (C) The fraction of normalized fluorescence recovery relative to row 2 is plotted (19 cells from 3 mice, mean ± SD). Cells are from the middle turn of the organ of Corti. **** denotes significance ($p < 0.0001$) and n.s. denotes no significance ($p > 0.05$).

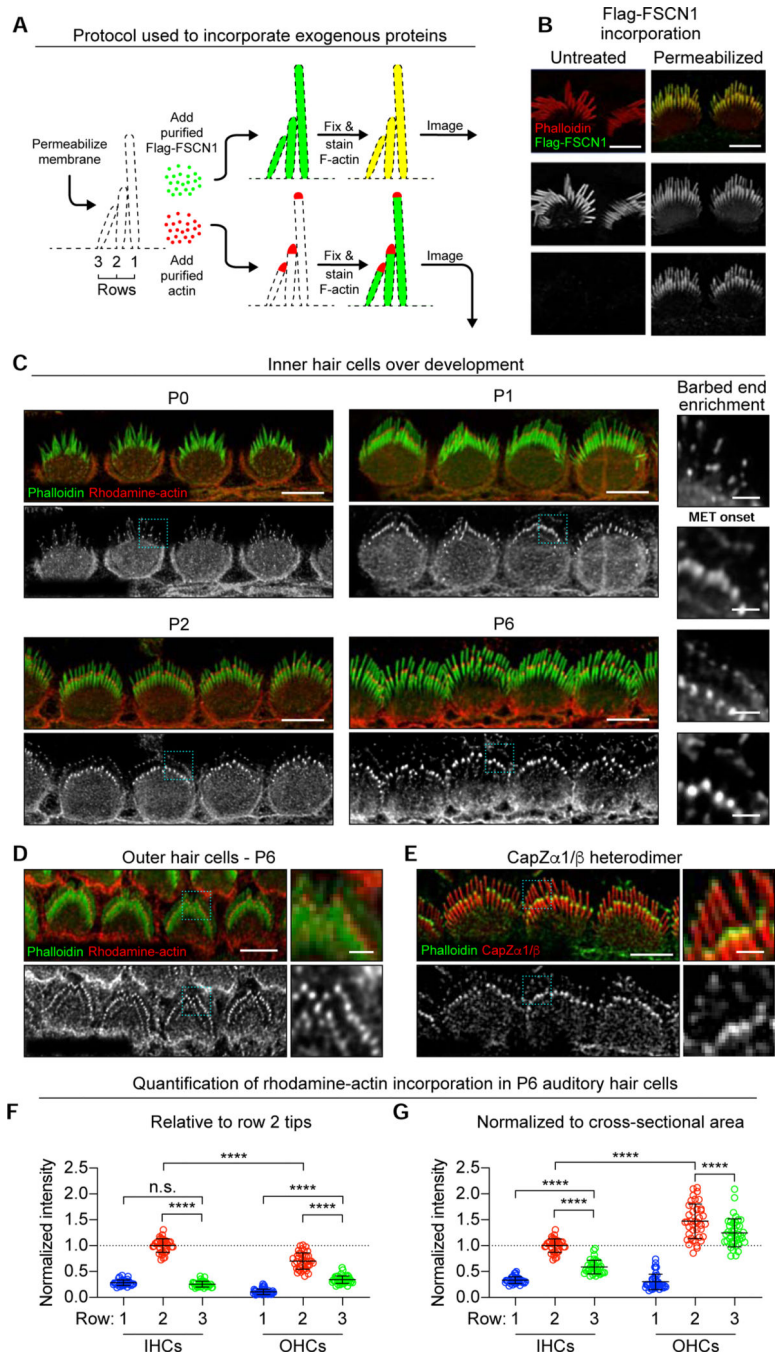

Figure 2. Rhodamine-labeled actin incorporation during postnatal development of auditory hair cells.

(A) A diagram outlining the assay where hair cells are permeabilized to allow purified proteins to access and bind to the underlying actin cytoskeleton. F-actin is stained with phalloidin. (B) Exogenous, purified Flag-FSCN1 was incubated with intact or permeabilized tissue at P5 and detected by an anti-Flag antibody (green). Endogenous F-actin was stained with phalloidin (red) to show inner hair cell (IHC) stereocilia. (C-D) Rhodamine labeled actin (red, grey) incorporation in permeabilized IHCs (C) at P0, P1, P2, and P6 or (D) P6 outer hair cells (OHCs). Endogenous F-actin was labeled with phalloidin (green).

Regions marked by boxes are magnified to the right, where the approximate onset of mechanotransduction (MET) is indicated. (E) Permeabilized P6 IHCs were labeled with exogenous, purified His-CAPZα1/β and detected by anti-His immunostaining (green, grey). Endogenous F-actin was stained with phalloidin (red). Scale bars in large rectangular images equal 5 μm and in small square images 1 μm. (F-G) Quantification of relative rhodamine-actin incorporation at the tips of rows 1, 2, and 3 (n = 35 to 42 cells from control mice). (F) Rhodamine-actin intensity at stereocilia tips normalized to the average intensity at row 2 tips. (G) The values of the graph in (F), normalized to the ratio of cross-sectional area between rows (0.85:1.00:0.43 for IHCs and 0.73:1.00:0.57 for OHCs; measured from scanning electron micrographs). Black bars in all graphs indicate mean ± SD. **** denotes significance ($p < 0.0001$) and n.s. denotes no significance ($p > 0.05$).

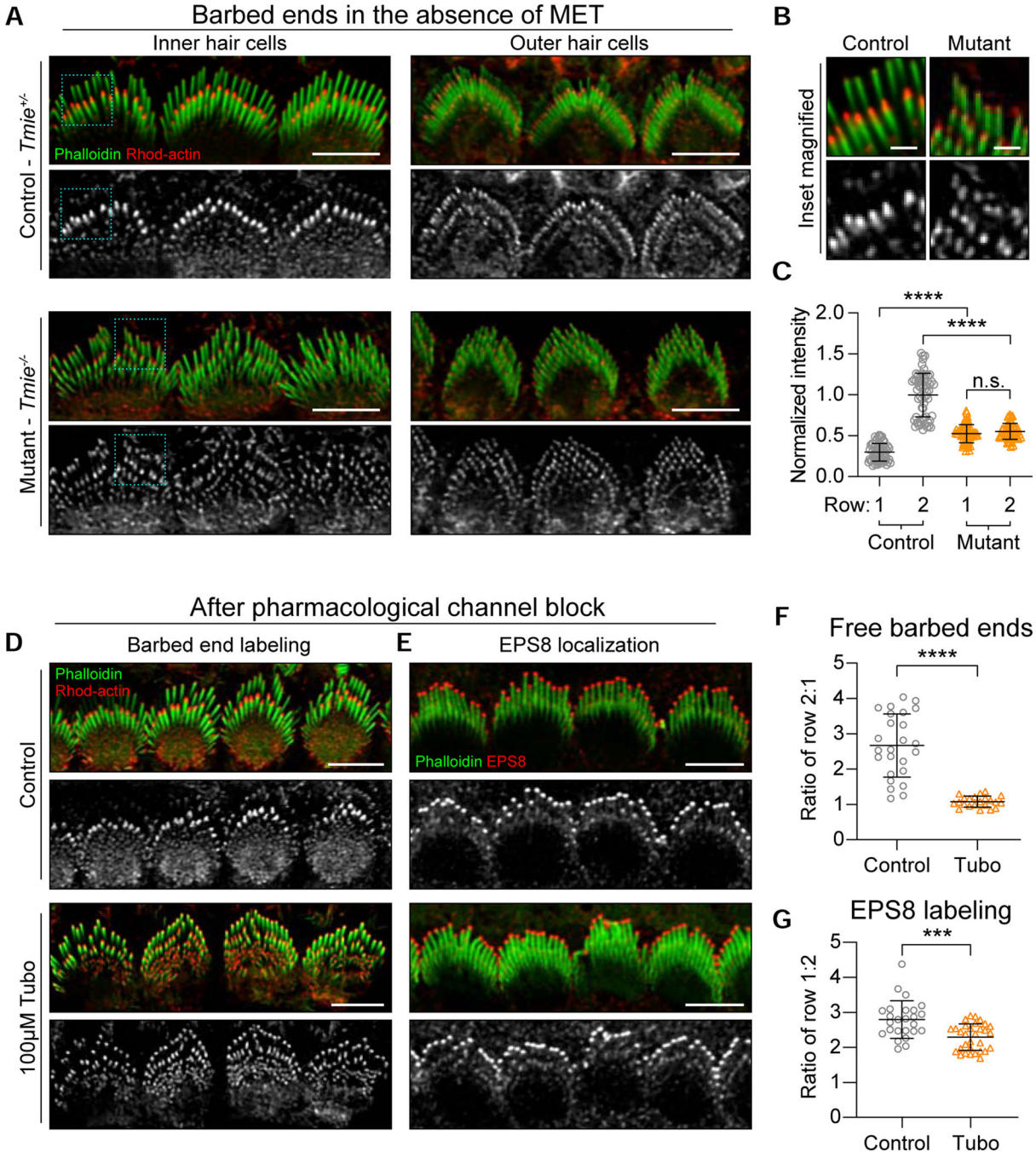

Figure 3. Rhodamine-labeled actin incorporation when mechantransduction is disrupted.

(A-B) Rhodamine-actin (red, grey) incorporation in permeabilized inner and outer hair cells of P6 *Tmie*$^{+/-}$ control and *Tmie*$^{-/-}$ mutant mice. Phalloidin stained F-actin is green. Boxed regions are magnified in (B). (C) The graph shows the normalized fluorescence intensity of rhodamine-actin at row 1 or row 2 stereocilia tips in *Tmie*$^{+/-}$ controls (n = 61 cells from 3 mice) and *Tmie*$^{-/-}$ mutants (n = 58 cells from 3 mice). Each data point represents the average tip intensity for each row of a cell normalized to the average intensity at cell borders. (D-G) P4 explants were incubated without (control) or with 100 µM tubocurarine

(Tubo) for 18 hours. (D) Rhodamine-actin incorporation (red, grey) and phalloidin stained F-actin (green). (E) EPS8 immunostaining (red, grey) and phalloidin stained F-actin (green). (F) Ratio of rhodamine-actin fluorescence intensities of row 2 to row 1 stereocilia tips from control (n = 25 cells from 3 mice) and Tubo treated explants (n = 22 cells from 3 mice). (G) Ratio of EPS8 fluorescence intensities of row 1 to row 2 stereocilia tips from control (n = 25 cells from 3 mice) and Tubo treated explants (n = 30 cells from 3 mice). Black bars in all graphs indicate mean ± SD. Each data point represents a cell. **** denotes significance ($p < 0.0001$); *** denotes significance ($p < 0.001$); n.s. denotes no significance ($p > 0.05$). Scale bars equal 5 μm in large squares and 1 μm in insets. All images are of hair cells from the middle turn. See also Figure S1.

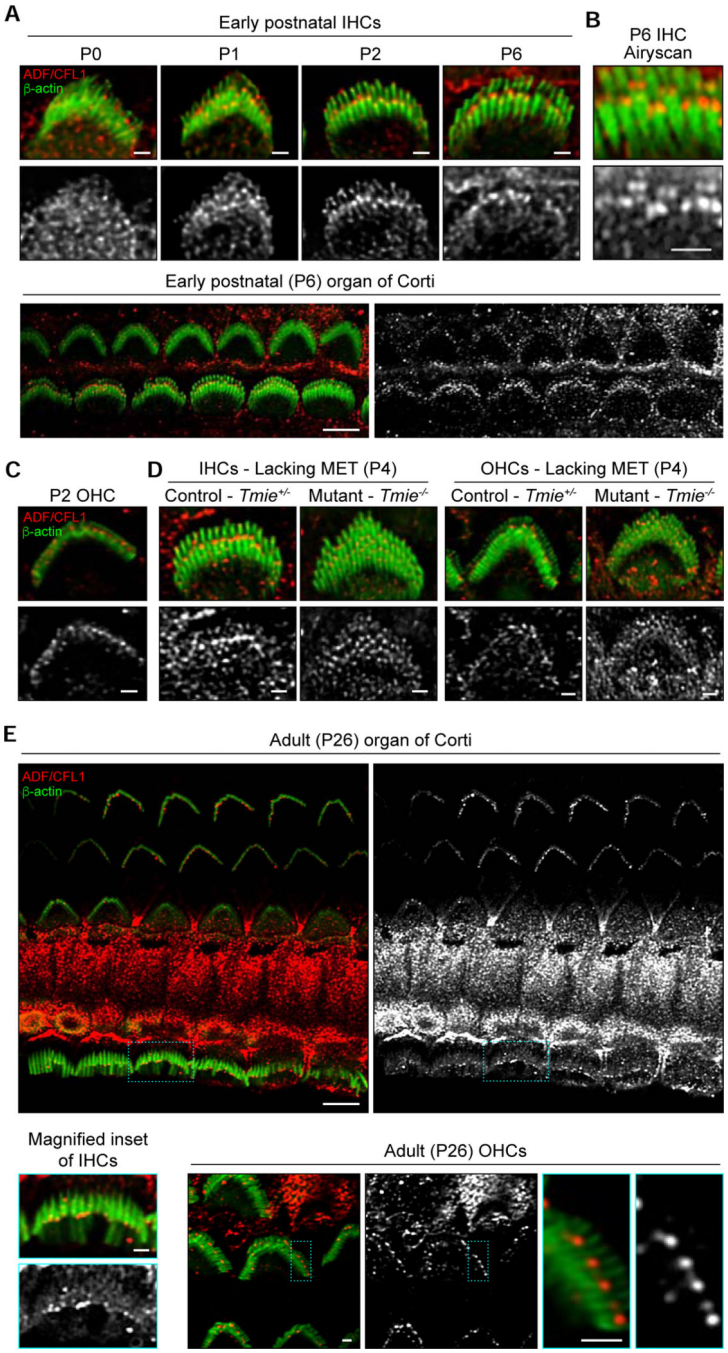

Figure 4. ADF/CFL1 localization in auditory hair cells.

(A-D) Immunolocalization of ADF/CFL1 (red or grey) and β-actin (green) during postnatal development. (A) Top panels, IHCs at P0, P1, P2, and P6. Bottom panels show ADF/CFL1 immunolocalization in the organ of Corti including both IHCs and OHCs. (B) P6 IHC stereocilia imaged by Airyscan microscopy. (C) P2 OHC stereocilia. (D) P4 *Tmie*$^{+/-}$ control and *Tmie*$^{-/-}$ mutant IHCs. (E) Immunolocalization of ADF/CFL1 (red or grey) and β-actin (green) in adult (P26) organ of Corti with a selected cell magnified below to better show

stereocilia labeling. Scale bars equal 5μm for the panels showing the sensory epithelium in (A) and (D), and 1μm for all other images.

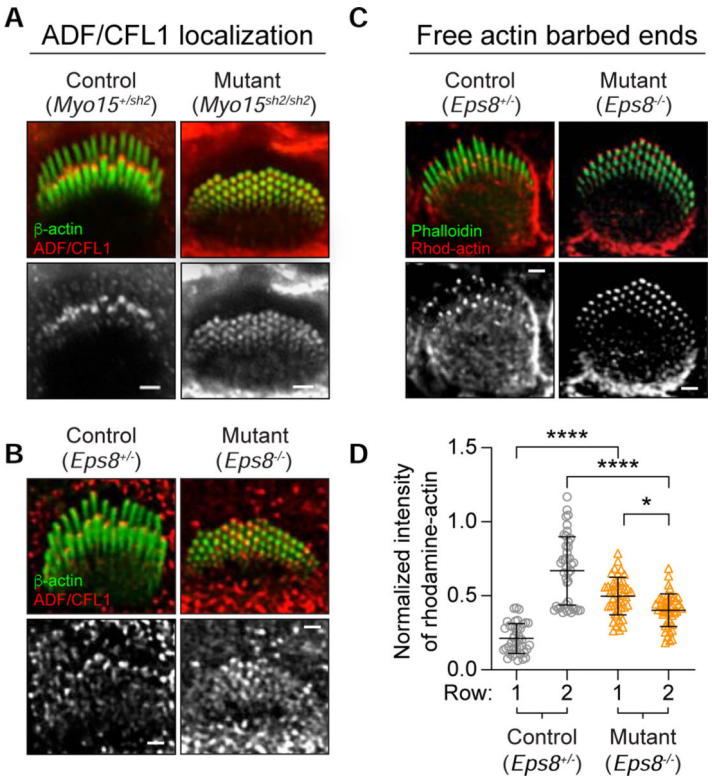

Figure 5. ADF/CFL1 localization and rhodamine-actin incorporation in *Myo15*$^{sh2/sh2}$ and *Eps8*$^{-/-}$ mutants.

(A) ADF/CFL1 immunolocalization (grey, red) in inner hair cells (IHCs) from P6 *Myo15*$^{+/sh2}$ controls and *Myo15*$^{sh2/sh2}$ mutants imaged by Airyscan or (B) P6 *Eps8*$^{+/-}$ control or *Eps8*$^{-/-}$ mutant IHCs. In merged images β-actin is green. (C) Rhodamine-actin (red or grey) incorporation in permeabilized P6 *Eps8*$^{+/-}$ control and *Eps8*$^{-/-}$ mutant IHCs. In the merged image, phalloidin stained F-actin is green. (D) Quantification of rhodamine-actin intensity at stereocilia tips normalized to border values for *Eps8*$^{+/-}$ controls (n = 42 cells from 3 mice) and *Eps8*$^{-/-}$ mutants (n = 44 cells from 3 mice). Black bars on the graph indicate mean ± SD. **** denotes significance ($p < 0.0001$) and * denotes significance ($p < 0.05$). All scale bars equal 1 μm. See also Figure S2 and STAR Methods.

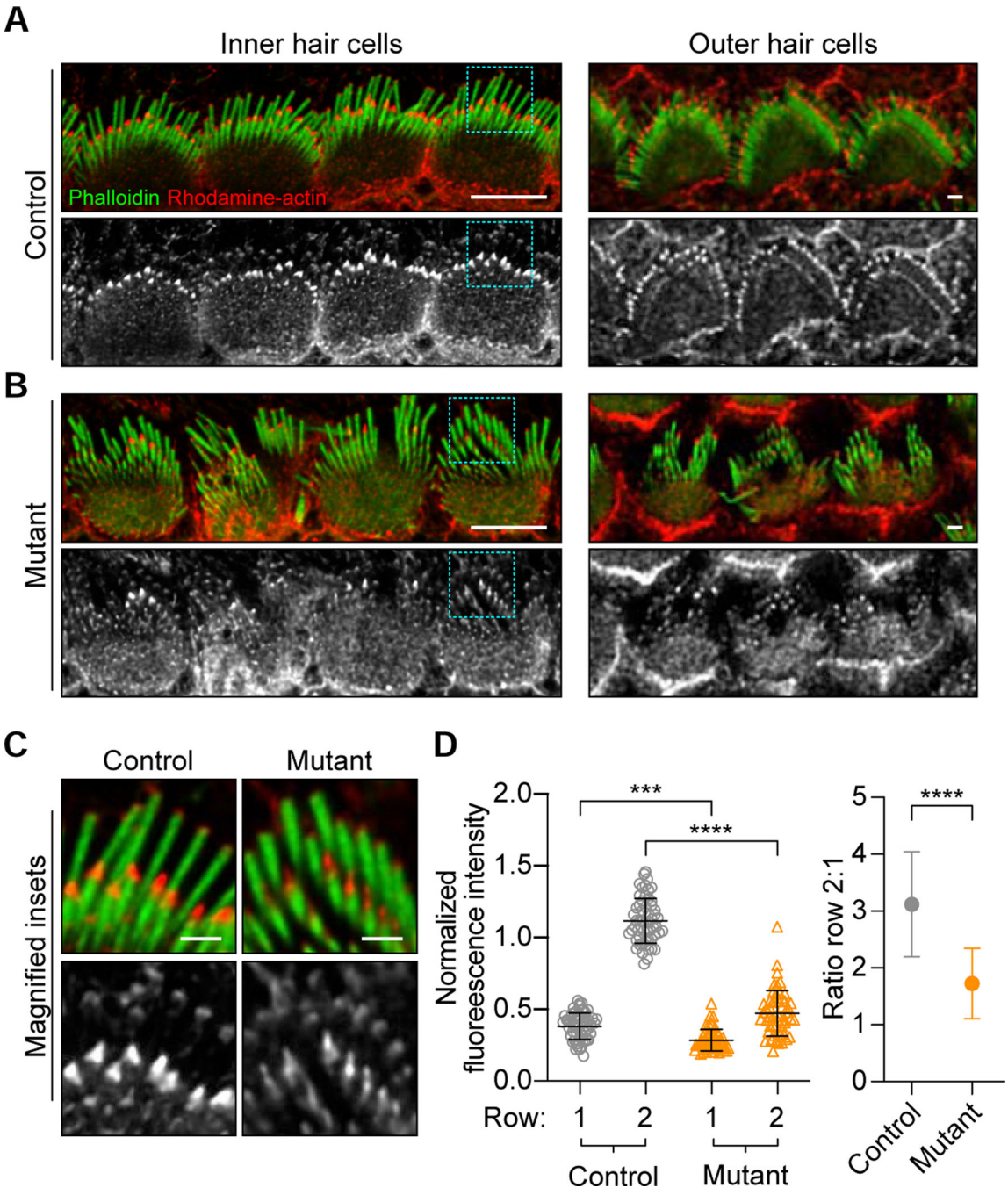

Figure 6. Rhodamine-actin incorporation in *Adf/Cfl1* mutants.

(A-C) Rhodamine-actin (red or grey) incorporation in permeabilized inner hair cells (IHCs) and outer hair cells (OHCs) of (A) P6 $Adf^{+/-}$ $CFL1^{fl/+}$ control or (B) $Adf^{-/-}$ $CFL1^{fl/+}$ *Atoh1-cre* mutant mice, which retain one intact allele of the *Cfl1* gene. Scale bars equal 5 μm and 1 μm for IHC and OHC panels, respectively. (C) Magnified insets of IHCs. (D) On the left, rhodamine-actin fluorescence intensity at row 1 and row 2 IHC stereocilia tips, normalized to the cell border. Each data point represents a cell and the black bars indicate mean ± SD. On the right, the mean ± SD of the ratio of rhodamine-actin fluorescence

intensities at row 2 stereocilia tips relative to row 1 from control and mutant hair cells. Control and mutant data points are colored grey and orange, respectively. Data represents 57 and 53 cells from 3 control and 4 mutant mice, respectively. **** denotes significance ($p < 0.0001$) and *** denotes significance ($p < 0.001$). See also Figure S3.

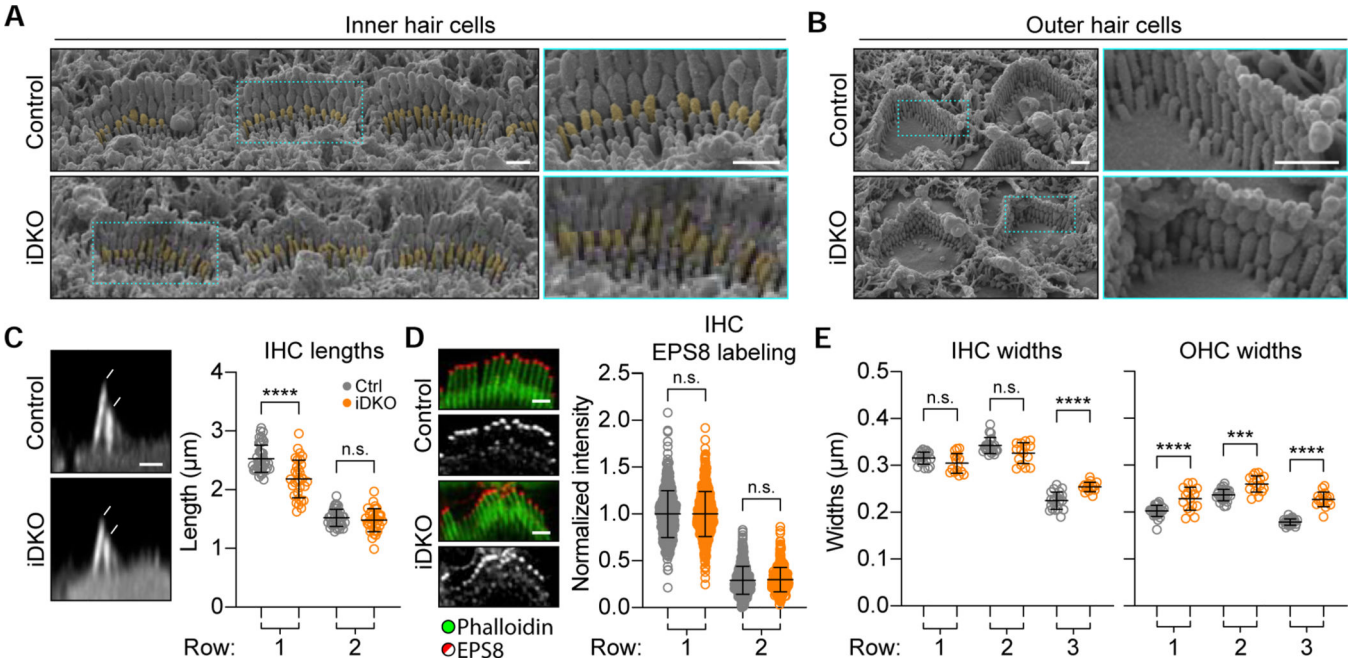

Figure 7. Stereocilia morphology in *Adf/Cfl1* induced double knockouts.

Adf$^{+/-}$ *Cfl1*$^{fl/+}$ mice (control) and *Adf*$^{-/-}$ *Cfl1*$^{fl/fl}$ *Cagg-creER* mice (induced double knockout, iDKO) were used at P5, three days after tamoxifen injection. (A) SEM micrographs of inner hair cell (IHC) stereocilia, note the tapered tip morphology in row 3 stereocilia of iDKO cells. Boxed regions are magnified to the right and row 3 stereocilia tips are highlighted by yellow pseudocolor. (B) SEM of outer hair cell (OHC) stereocilia from control and iDKO mice, boxed regions magnified to the right. (C) Stereocilia lengths for control and iDKO IHCs were measured from digitally resliced image stacks to show the z dimension. On the left, representative resliced images from controls (top) and iDKO mutants (bottom). The graph shows length measurements for each condition with each data point representing a cell. For each condition, 35 to 40 cells were measured from four mice. (D) EPS8 immunostaining and quantification. Data points represent stereocilia and have been normalized to the average row 1 intensity. For each condition, 361 to 503 stereocilia per row were measured from an average of 7.75 cells from each of four mice. (E) Widths of IHC (left) and OHC (right) stereocilia were quantified from the widest, visible portion of each stereocilium from scanning electron micrographs. For IHCs, 15–21 cells from each condition were measured. For OHCs, 16–27 cells were measured. Two mice were used for each condition. Black bars in all graphs indicate mean ± SD. All scale bars equal 1 µm. See also Figures S4 and S5.

KEY RESOURCES TABLE

REAGENT or RESOURCE	SOURCE	IDENTIFIER
Antibodies		
Rabbit anti-CFL1 Monoclonal Primary Antibody	Cell Signaling Technologies	RRID:AB_10622000, Cat.# 5175
Mouse anti-β-actin Monoclonal Primary Antibody Conjugated to FITC	Abcam	RRID:AB_305394, Cat.# ab6277
Mouse anti-EPS8 Monoclonal Primary Antibody	BD Biosciences	RRID:AB_397544, Cat.#610143
Goat anti-mouse Alexa488 Secondary Antibody	Invitrogen	RRID:AB_138404, Cat.# A11029
Goat anti-mouse Alexa546 Secondary Antibody	Invitrogen	RRID:AB_143051, Cat.# A11035
Goat anti-mouse Alexa568 Secondary Antibody	Invitrogen	RRID:AB_10563566, Cat.# A11036
Goat anti-mouse Alexa488 Secondary Antibody	Invitrogen	RRID:AB_141725, Cat.# A21236
Alexa488-labeled Phalloidin	Invitrogen	Cat.# A12379
Mouse anti-FLAG Monoclonal Antibody	Sigma	RRID:AB_259529, Cat.# F3165
Mouse anti-His Monoclonal Antibody Congugated to iFluor488	GenScript	Cat.# A01800
Chemicals, Peptides, and Recombinant Proteins		
Nuclease Free Duplex Buffer	Integrated DNA Technologies	Cat.# 11–01-03–01
Paraformaldehyde Aqueous Solution (16%)	Electron Microscopy Sciences	Cat.# 15710
Triton X-100	Sigma Aldrich	Cat.# X-100–100ML
Dulbecco's Modified Eagle Medium (DMEM) and Ham's F-12 nutrient mixture buffered with HEPES	Thermo Fisher Scientific	Cat.# 11039047
Hank's Buffered Saline Solution (HBSS) Containing Calcium and Magnesium	Thermo Fisher Scientific	Cat.# 14025092
ProLong Diamond Antifade Mountant	Thermo Fisher Scientific	Cat.# P36961
SF900 III SFM	Thermo Fisher Scientific	Cat.# 12658019
Ready-to-use Glutaraldehyde 2.5% in 0.1M Sodium Cacodylate Buffer, pH 7.4	Electron Microscopy Sciences	Cat.# 16537–15
Fast Green FCF	Thermo Fisher Scientific	Cat.# BP123–10
Recombinant *Streptococcus pyogenes* Cas9 Nuclease	Integrated DNA Technologies	Cat.# 1081058
Adenosine 5′-triphosphate disodium salt trihydrate	Sigma Aldrich	Cat.# 10127531001
Sodium pyruvate	Thermo Fisher Scientific	Cat.# BP356–100
Penicillin G sodium salt	Sigma Alrich	Cat.# P3032–10MU
Human Epidermal Growth Factor	Sigma Aldrich	Cat.# E9644–0.2MG
Human Fibroblast Growth Factor, Basic	Simga Aldrich	Cat.# F0291–25UG
Insulin-like Growth Factor-I from Mouse	Sigma Aldrich	Cat.# I8779–50UG
Heparan sulfate proteoglycan	Sigma Aldrich	Cat.# H4777-.1MG
N-2 Supplement	Sigma Aldrich	Cat.# 17504048
B-27 Supplement, Serum Free	Thermo Fisher Scientific	Cat.# 17504044
Tubocurarine hydrochloride pentahydrate	Sigma Aldrich	Cat.# T2379–100MG

REAGENT or RESOURCE	SOURCE	IDENTIFIER
Tannic acid	Electron Microscopy Sciences	Cat.# 21710
2% Osmium tetroxide	Electron Microscopy Sciences	Cat.# 19152
Saponin Extract	Simga Aldrich	Cat.# S4521
Rhodamine-labeled Rabbit Muscle Actin	Cytoskeleton, Inc.	Cat.# AR05
Experimental Models: Organisms/Strains		
Mouse: Cagg-creER: Tg(CAG-cre/Esr1*)5Amc	The Jackson Laboratory	MGI:2182767, JAX:004682, RRID:IMSR_JAX:017595
Mouse: Adf$^{-/-}$: B6.Cg-Dstn^{corn1}	Gift from Ikeda Lab	MGI:1889311
Mouse: Cfl1$^{fl/fl}$: Cfl1tm1.1Wit	Gift from Walter Witke and Christine Gurniak	MGI:4943295
Mouse: B6: C57BL/6J	The Jackson Laboratory	MGI:3028467, JAX:000664
Mouse: β-actin-EGFP: C57BL/6-Tg(CAG-tdTomato,Actb/EGFP)1Erv/J	The Jackson Laboratory	MGI:5810463, JAX:029889
Mouse: EGFP-β-actin: C3;129S7-Hprt^{tm2Brd}/Biat	Gift from Haydn Prosser	MGI:5561057
Mouse: Myo15$^{sh2/sh2}$: Myo15^{sh2}	Thomas Friedman	MGI:1857036, JAX:000109, RRID:IMSR_JAX:011104
Mouse: Tmie$^{-/-}$:Tmie^{tm2Mull}	Bo Zhao	MGI:5784557
Mouse: Atoh1-cre: Tg(Atoh1-cre)1Bfri	The Jackson Laboratory	MGI:3775845, JAX:004682, RRID:IMSR_JAX:000109
Oligonucleotides		
Primer: 5'-ACCGGTACACTTTGCAAACAAGA-3'	N/A	N/A
tracrRNA	Integrated DNA Technologies	Cat.# 1072534
crRNA targeting *Eps8*: TGACCACCTTCGTGCTGGATCGG	N/A	N/A
crRNA targeting *Tyr*: TGACCACCTTCGTGCTGGATCGG	N/A	N/A
Primer: 5'-AATACTATGCTGTTGCAGCCCC-3'	N/A	N/A
Recombinant DNA		
Plasmid, 6XHis-tagged CapZα1/β heterodimer construct	Addgene	Plasmid# 89950, http://n2t.net/addgene:89950, RRID:Addgene_89950
cDNA clone, Human *Fscn1*	Gift from Steve Almo	N/A
Software and Algorithms		
GraphPad Prism 8	GraphPad	RRID:SCR_002798; https://www.graphpad.com/scientific-software/prism
Adobe Photoshop	Adobe	RRID:SCR_014199; https://www.adobe.com/products/photoshop.html
Leica Application Suite X	Leica Microsystems	RRID:SCR_013673, https://www.leica-microsystems.com/products/microscope-software/details/product/leica-las-x-ls/
ImageJ (FIJI)	NIH	RRID:SCR_002285; https://fiji.sc/
Adobe Illustrator	Adobe	RRID:SCR_010279, http://www.adobe.com/products/illustrator.html

REAGENT or RESOURCE	SOURCE	IDENTIFIER
Zeiss Zen Black software v2.3 SP1 FP3, 64-bit	Carl Zeiss Microscopy LLC, Germany	RRID:SCR_013672, http://www.zeiss.com/microscopy/en_us/products/microscope-software/zen.html#introduction
Microsoft Excel (v16.41)	Microsoft Corporation	RRID:SCR_016137, https://www.microsoft.com/en-us/microsoft-365/excel
Other		
Zeiss Airyscan LSM 880	Carl Zeiss Microscopy LLC, Germany	N/A
60×15mm CytoOne Dish, TC-Treated	USA Scientific	Cat.# CC7682–3359
25mm Glass Coverslip	Fisherbrand	Cat.# 12–545-102 25CIR
Minutien Pins	Fine Science Tools	Cat.# 26002–20
Sylgard 184	Electron Microscopy Sciences	Cat.# 24236–10
35×10mm CytoOne Dish, TC-Treated	USA Scientific	Cat.# CC7682–3340
Platinum Tweezertrode, 3 mm Diameter	BTX Molecular Delivery Systems	Cat.# 45–0487
24-well Polystyrene Culture Microplates	Thermo Fisher Scientific	Cat.# 08–772-1
Tousimis Samdri-780 Critical Point Dryer	Tousimis Reseach Corporation	https://tousimis.com/
JEOL 7800F Schottky Field Emission Scanning Electron Microscope	JEOL	https://www.jeol.co.jp/en/products/detail/JSM-7800F.html
BTX ECM 830 Square Wave Electroporation System	BTX Molecular Delivery Systems	Cat.# 45–0662
Leica SP8 Inverted Confocal Microscope	Leica Microsystems	RRID:SCR_018169, https://www.leica-microsystems.com/products/confocal-microscopes/p/leica-tcs-sp8/)